Ludwig-Maximilians-Universität München
Faculty of Physics

Master Thesis

Upgrading the Cosmic Ray Facility for Tests of the Phase-II Upgrade of the ATLAS Muon Spectrometer

submitted by

Florian Egli

born in Rosenheim

Supervisor: Prof. Dr. Otmar Biebel

Munich, 22 May 2023

Ludwig-Maximilians-Universität München
Fakultät für Physik

Masterarbeit

Upgrade der Cosmic Ray Facility für Tests des Phase-II Upgrades des ATLAS Myonenspektrometers

vorgelegt von

Florian Egli

geboren in Rosenheim

Gutachter: Prof. Dr. Otmar Biebel

München, 22. Mai 2023

Abstract

The Phase-II Upgrade of the ATLAS Muon Spectrometer for High Luminosity LHC includes the installation of a new and more efficient trigger and readout system for the Monitored Drift Tube (MDT) chambers. It is crucial that the Phase-II Upgrade can be tested on MDT chambers outside of ATLAS, to detect errors and verify possible solutions in advance, independent of the upgrade operations at CERN. The Cosmic Ray Facility (CRF) in Garching could provide an ideal test site, as it consists of up to three fully functional MDT chambers. However, its readout electronics and infrastructure are currently not compatible with the Phase-II Upgrade. As a first step, the infrastructure and electronics in the Cosmic Ray Facility were upgraded to the current standard of the ATLAS Muon Spectrometer. This includes the setup of a FELIX-MROD based readout system, which is compatible with both the current and the Phase-II MDT electronics. Furthermore, it is necessary to ensure backward compatibility with the legacy system of the CRF, in order to make use of the plethora of analysis scripts that are already in place. This includes the conversion between different data formats and custom event building. Finally, the new readout system is validated by comparison with Garfield++ simulations, studies about MDT performance in ATLAS and the readout with the CRF legacy system.

Kurzfassung

Das Phase-II Upgrade des ATLAS Muon Spektrometers zum High Luminosity LHC beinhaltet die Installation eines neuen und effizienteren Trigger- und Auslese-Systems für die Monitored Drift Tube (MDT) Kammern. Es ist entscheidend, dass das Phase-II Upgrade an MDT Kammern außerhalb von ATLAS getestet werden kann, um Fehler zu erkennen und mögliche Lösungen unabhängig von den Upgradearbeiten am CERN im Vorfeld zu verifizieren. Die Cosmic Ray Facility (CRF) in Garching kann hierfür eine ideale Testumgebung bieten, da sie aus bis zu drei voll funktionsfähigen MDT Kammern besteht. Allerdings sind die Ausleseelektronik und Infrastruktur derzeit nicht mit dem Phase-II Upgrade kompatibel. Als erster Schritt wurde daher die Infrastruktur und Elektronik der Cosmic Ray Facility auf den Phase-I Standard des ATLAS Muon Spektrometers aktualisiert. Dies beinhaltet die Einrichtung eines FELIX-MROD-basierten Auslese-Systems, das mit sowohl der derzeitigen als auch der Phase-II Elektronik kompatibel ist. Des Weiteren ist es notwendig, die Rückwärtskompatibilität zum bestehenden System der CRF sicherzustellen, um von der Vielzahl der bereits vorhandenen Analyse-Skripte Gebrauch machen zu können. Hierzu gehört die Konvertierung zwischen verschiedenen Datenformaten sowie der Event-Aufbau. Schließlich wird das neue Auslese-System durch den Vergleich mit Garfield++ Simulationen, Studien zur MDT-Performance in ATLAS sowie dem bestehenden System validiert.

Contents

1. Introduction

1.1. The ATLAS Experiment at CERN

The ATLAS[1] detector is one of two general-purpose detector systems at the Large Hadron Collider (LHC) at CERN. In the center of the cylindrical setup, particle beams from the LHC collide and create new particles, which can be detected by the detector. This way, a wide range of physics can be investigated: both standard model physics such as the Higgs boson as well as searches for physics beyond the standard model. The ATLAS detector consists of six detector subsystems [CERN 2023]. The outermost subsystem is the Muon Spectrometer.

1.1.1. The Muon Spectrometer

The ATLAS Muon Spectrometer consists of three large superconducting toroidal magnets: two in the end caps and one air-core magnet in the barrel region. They provide a field of approximately 0.5 T. The bending of the muon trajectories is measured with three layers of high-precision tracking chambers, which are triggered by separate RPC/TGC chambers. The original design of the Muon Spectrometer and its detector systems is shown in Fig. 1.1. In both, the barrel and the end cap of the cylinder, gaseous detectors called Monitored Drift Tube (MDT) chambers are used as precision trackers. Only in the innermost layer of the end cap, where radiation levels are especially high, different detectors with high rate capabilities have to be used. In the original design Cathode Strip Chambers (CSCs) were used for this purpose [The ATLAS Collaboration 2008, 2017].

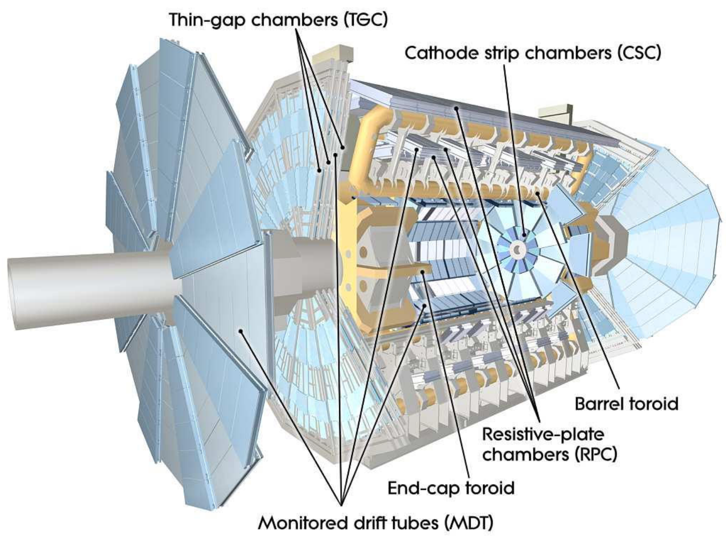

Figure 1.1.: Cut-away view of the ATLAS muon spectrometer, before the High-Luminosity Upgrades. Figure taken from [The ATLAS Collaboration 2008].

[1] A Toroidal LHC ApparatuS

1.1.2. The Phase-II Upgrade

The LHC was designed to deliver proton-proton collisions at a centre-of-mass energy of $\sqrt{s} = 14\,\mathrm{TeV}$ at an instantaneous luminosity of $1 \times 10^{34}\,\mathrm{cm}^{-2}\,\mathrm{s}^{-1}$. Already in 2018, a peak luminosity of $2 \times 10^{34}\,\mathrm{cm}^{-2}\,\mathrm{s}^{-1}$ was achieved, twice the design value [Steerenberg 2018; The ATLAS Collaboration 2017].

In order to fully exploit the physics potential of LHC, further increases in the luminosity are planned in the High Luminosity LHC (HL-LHC) project. Its aim is to achieve a peak luminosity of $7.5 \times 10^{34}\,\mathrm{cm}^{-2}\,\mathrm{s}^{-1}$. This will ultimately accumulate about $4000\,\mathrm{fb}^{-1}$ of integrated luminosity [The ATLAS Collaboration 2017]. For the present timetable of HL-LHC, see Fig. 1.2.

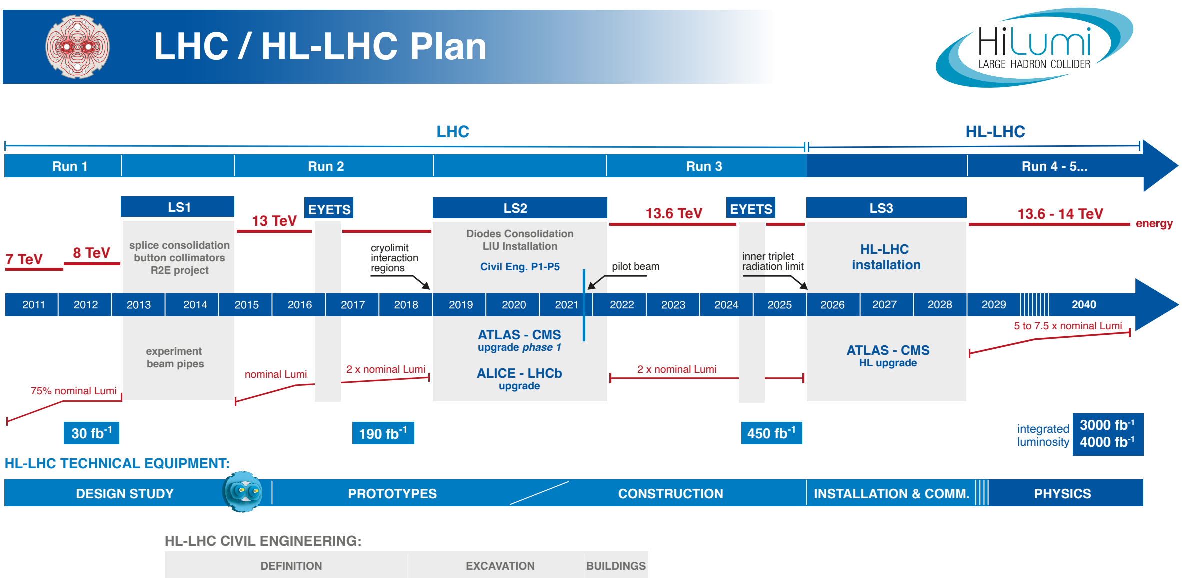

Figure 1.2.: The schedule for HL-LHC. Taken from [HL-LHC Collaboration 2023].

The increased luminosity will lead to an increase in particle fluxes by the same factor. It must be ensured that ATLAS can operate at the increased luminosity without significant performance loss. The existing detector systems were designed for operation at $1 \times 10^{34}\,\mathrm{cm}^{-2}\,\mathrm{s}^{-1}$ and must therefore be upgraded. This upgrade is split into two phases. During Phase-I, the Muon Spectrometer end caps received the New Small Wheel upgrade. The innermost layers, the old Small Wheel, which contained the CSCs, was replaced with high-rate capable Micromegas detectors for precision tracking [Nicolás Viaux 2023].

In Phase-II of the upgrade, the MDT chamber front-end and readout electronics, as well as the trigger system will be completely redesigned [The ATLAS Collaboration 2017].

It is essential that the Phase-II electronics and trigger for the MDT chambers can be tested in advance on an MDT chamber setup outside of ATLAS, to detect errors and verify solutions. An ideal test site is the Cosmic Ray Facility in Garching.

1.2. The Cosmic Ray Facility in Garching

The Cosmic Ray Facility (CRF) is a detector system in Garching that is used to detect cosmic muons. It consists of two MDT chambers for precision reference tracking of the muons as well as three layers of segmented scintillators, one on the top and two on the bottom of the setup, for triggering the readout system. The MDT chambers are of the BOS type, as used in the outer barrel layer of the ATLAS Muon Spectrometer. The setup is shown in Fig. 1.3.

Figure 1.3.: Picture of the Garching Cosmic Ray Facility. Shown are the two MDT reference chambers, as well as the photomultipliers of one of the layers of the lower hodoscope. The scintillators of the upper hodoscope are hidden behind the structure, on top of the silver "top plate" of the CRF. Between the two MDT chambers, a slot allows for the insertion of a third chamber. The wire positions of more than 100 BOS chambers delivered to CERN have been calibrated in this setup. The resolution was 8 µm in precision direction and 20 µm in perpendicular direction. Taken from [LMU Munich 2023].

Historically the CRF has been used for the commissioning and precision calibration of BOS detectors for the ATLAS experiment at CERN: The two reference MDTs and the scintillators allow for the construction of reference tracks, which can be used to test a detector that is inserted in the free slot between the MDT chambers.
From 2000 to 2006 the BOS MDT chambers, which were produced in Munich, were tested and commissioned with the CRF. After that, gas studies and thermal deformation studies were performed. Beginning in 2013 and still ongoing, it was used for the testing of Micromegas chambers: At first systematic studies were made with prototypes. Then, until 2021, the SM2 (Small Module 2) chambers for the ATLAS New Small Wheel were tested and precision calibrated. From 2021 to the present it is used for systematic studies on Micromegas modules and the calibration of two spare SM2 modules for the NSW.[2]

Before this work was started, the infrastructure of the CRF was incompatible with the electronics used in the ATLAS Muon Spectrometer. Thus, it could not be used for tests of the Phase-II Upgrade. In this work, the CRF is upgraded to the current standard of ATLAS MDT electronics. This involves the setup of a FELIX-MROD based readout system.

This work is structured as follows. Since Monitored Drift Tubes are gaseous detectors, a general introduction to the physics of gaseous detectors will be given in chapter 2. In chapter 3, an overview of the structure and processes in MDT Chambers will be provided. The MDT electronics, as they are currently employed in the ATLAS detector, are presented in chapter 4. Finally, the upgrade operations at the Cosmic Ray Facility will be explained in chapter 5 and validated in chapter 6. The conclusion and outlook in chapter 7 conclude this work.

[2]O. Biebel and R. Hertenberger, private communication.

2. Physical Processes inside Gaseous Detectors

The detectors discussed in this thesis, the so-called Monitored Drift Tube (MDT) chambers, are an assembly of cylindrical gaseous detectors. Before we focus on MDT chambers in chapter 3, the physical processes that make particle detection with gaseous detectors possible are discussed here.

Particle detectors take advantage of the fact that charged particles traversing matter transfer part or all of their energy to the medium. They are designed such that this energy transfer can be detected [Sauli 2023]. For large-area applications, such as the ATLAS Muon Spectrometer, gaseous detectors are well suited. An incident charged particle, like a muon, transfers part of its energy to the gas molecules, some of which become ionized. These ionization events can be detected by applying an electric field: This causes the electrons and ions to become separated and drift towards the anode and cathode, respectively, where they can be picked up and measured as a current. To increase the signal, to a level where it is measurable, the process of gas amplification is often used, increasing the number of electrons and ions reaching the detection electrodes by a factor of 1×10^3 to 5×10^5.

In this chapter, first the interaction of charged particles heavier than electrons with matter is discussed. Then, the thermal diffusion and the drift of the electrons and ions under the influence of electric fields are explained, followed by the section about gas amplification. Finally, the special case of cylindrical gaseous detectors and their operation regimes in dependence on the applied voltage is considered.

2.1. Interaction of Charged Particles with Matter

For heavy charged particles, like muons, the largest fraction of the transferred energy is due to electromagnetic interaction, which mainly results in excitation and ionization of the atoms and molecules in the medium [Sauli 2023].

The average rate of energy loss per unit length in the material is described by the Bethe-Bloch equation

$$\left\langle -\frac{\mathrm{d}E}{\mathrm{d}x} \right\rangle = 4\pi N_A r_e^2 m_e c^2 \rho z^2 \frac{Z}{A} \frac{1}{\beta^2} \left[\frac{1}{2} \ln \frac{2 m_e c^2 \beta^2 \gamma^2 W_{\max}}{I^2} - \beta^2 - \frac{\delta(\beta\gamma)}{2} \right] \tag{2.1}$$

where N_A is the Avogadro constant, $r_e = \frac{e^2}{4\pi\varepsilon_0 m_e c^2}$ the classical electron radius, m_e the electron mass, c the speed of light, ρ the density of the material traversed, z the charge number of the incident particle, Z the atomic number and A the atomic mass of the medium, $\beta = v/c$ the velocity of the incident particle, $\gamma = 1/\sqrt{1-\beta^2}$ the Lorentz factor, $W_{\max}$ the maximum possible energy transfer to an electron in a single collision, I the mean excitation energy and $\delta(\beta\gamma)$ the density effect correction to ionization energy loss [Particle Data Group et al. 2022].

The mass stopping power $\frac{\mathrm{d}E}{\rho \cdot \mathrm{d}x}$ for a positive muon in copper is shown in Fig.2.1. Except in hydrogen, particles with the same speed have similar rates of energy loss in different materials. Cosmic muons have their energy loss rate close to the minimum of the distribution, at $\beta\gamma \approx 4$

[Particle Data Group et al. 2022]. As a consequence, they are not stopped inside a gaseous detector but do ionize the gas molecules along their track.

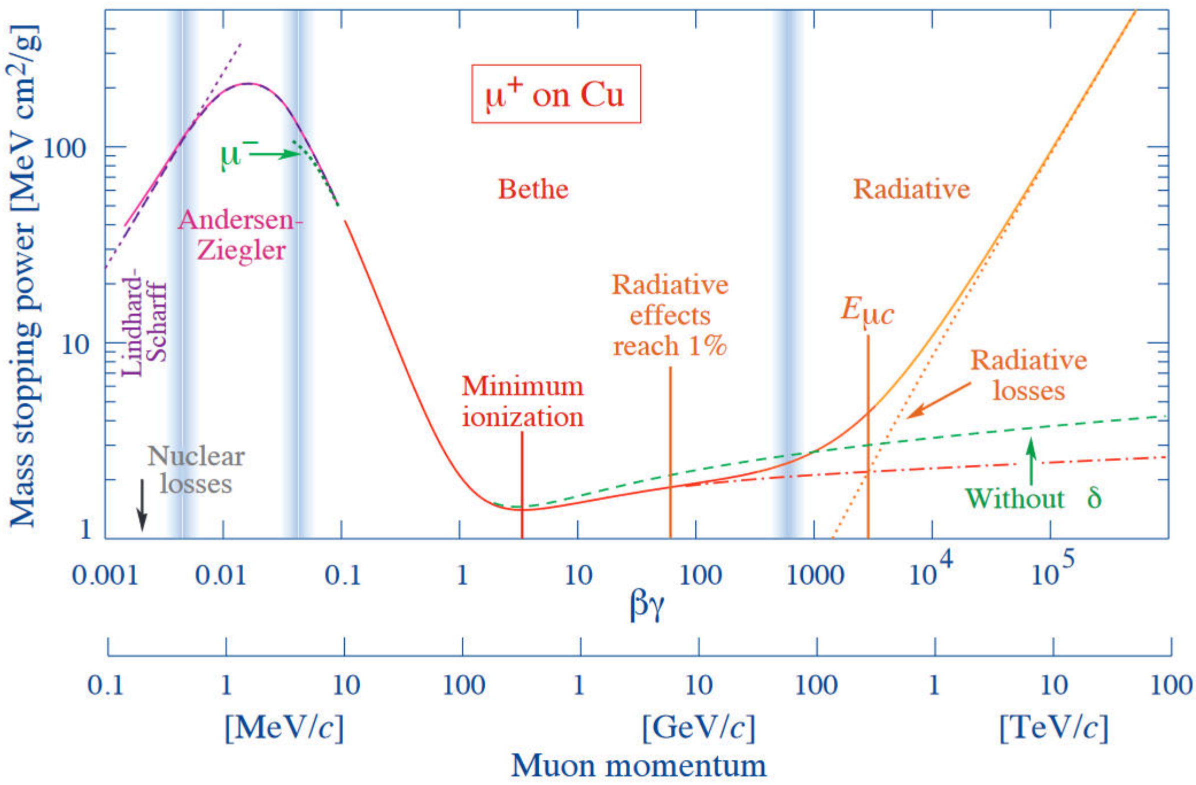

Figure 2.1.: Average mass stopping power for positive muons in copper as a function of $\beta\gamma$ and muon momentum. The solid curves indicate the total stopping power. At $\beta\gamma \approx 4$, there is an ionization minimum. Taken from [Particle Data Group et al. 2022].

2.2. Drift and Diffusion of Charges in Gases

Part of the transferred energy of the muon will cause ionization events, creating electron-ion pairs. These electrons and ions quickly thermalize with the atoms and molecules of the surrounding gas. In the absence of electric fields, their movement in the gas is described by diffusion equations. In the presence of moderate electric fields, an average drift motion of the charged particles along the electric field lines is observed.

The movement of the charges through the gas can be cut short by neutralization in the gas or at the container walls. Ions can be neutralized by charge transfer with a molecule of its own gas or of a species with a smaller ionization potential. Electrons can be captured by positive ions, attach to a molecule with electron affinity, such as water, or be absorbed by the walls of the container [Sauli 2023].

2.2.1. Thermal Diffusion

If no external fields are present and inelastic collision processes can be ignored, ions and electrons produced in the gas can be described by the classic kinetic theory of gases. Therefore, their velocities v follow the Maxwell-Boltzmann distribution

$$f(v) = 4\pi \left(\frac{m}{2\pi k_B T} \right)^{\frac{3}{2}} v^2 \exp\left[-\frac{mv^2}{2k_B T} \right], \tag{2.2}$$

where m is the mass of the electron or ion, k_B is the Boltzmann constant, and T is the temperature [Sauli 2023].

The average velocity is

$$\bar{v} = \sqrt{\frac{8k_B T}{\pi m}}. \tag{2.3}$$

The linear diffusion of a localized distribution of ions or electrons takes place symmetrically, following a Gaussian law:

$$\frac{\mathrm{d}N}{N} = \frac{1}{\sqrt{4\pi Dt}} \exp\left(-\frac{x^2}{4Dt} \right) \mathrm{d}x \tag{2.4}$$

where $\mathrm{d}N/N$ is the fraction of particles in the element $\mathrm{d}x$ at a distance x from the origin after a time t and $D = \frac{1}{3}\bar{v}\lambda$ is the diffusion coefficient, which is determined by the average velocity $\bar{v}$ and the mean free path λ of the electron or ion in the gas. For one-dimensional diffusion this results in a spread of

$$\sigma_x(t) = \sqrt{2Dt}, \tag{2.5}$$

which is a function of the diffusion coefficient D and the time t. For spherical diffusion in three dimensions, the standard deviation describing the ion or electron concentration is given by [Leo 1994; Sauli 2023]

$$\sigma_V(t) = \sqrt{6Dt}. \tag{2.6}$$

The thermal diffusion of electrons and ions can be described by the same set of formulas. However, due to the large differences in mass, the drift motion has to be considered for ions and electrons separately.

2.2.2. Ion Drift

In the presence of an electric field E, in addition to the symmetric diffusion, a net movement of the ions along the field direction is observed. The average velocity of this motion is called the drift velocity w^+. For ions, up to very high fields, it is slow compared to the random thermal motion velocities.It is linearly proportional to the reduced electric field E/p up to high values of E. This motivates the definition of the ion mobility μ as

$$\mu = \frac{w^+}{E}, \tag{2.7}$$

which is constant at constant pressure [Leo 1994]. It depends on the particle type and is a function of temperature and pressure by eq. (2.8) [Sauli 2023].

$$\mu(P,T) = \frac{T}{T_0}\frac{P_0}{P}\mu(P_0,T_0)\;. \tag{2.8}$$

For ideal gases, in which the moving ions stay in thermal equilibrium with the gas, the ion mobility μ and the diffusion coefficient D can be shown to be related by the Nernst-Townsend formula

$$\frac{D}{\mu} = \frac{k_B T}{e}\,, \tag{2.9}$$

where k_B is the Boltzmann constant and e the electron charge [Leo 1994; Sauli 2023]. The diffusion spread of the ions along the drift direction is then obtained by plugging (2.9) into (2.5)

$$\sigma_x(t) = \sqrt{\frac{2k_B T}{e}\cdot\mu\cdot t}\,. \tag{2.10}$$

By application of (2.7), one can obtain the spread as a function of the drift distance $x = w^+ \cdot t$, as given in [Sauli 2023]:

$$\sigma_x(x) = \sqrt{\frac{2k_B T}{e}\frac{x}{E}}\,. \tag{2.11}$$

Note that the diffusion caused by the drift, as a function of x, only depends on the electric field and the temperature, but not the ion type, mass, or pressure [Sauli 2023]. However, as a function of the drift time t, it does depend on ion type, mass and pressure through the mobility μ.

2.2.3. Electron Drift

Like ions, electrons quickly reach thermal equilibrium with the surrounding gas molecules. Due to their lower mass, their thermal velocity is several orders of magnitude higher than that of the ions, as can be seen from Eq. (2.3). It follows from the definition of D and (2.6), that their thermal diffusion occurs much faster than that of the ions.

In the presence of an electric field, the electrons move in the opposite direction of the field vector.

The electron drift velocity is described by

$$w^- \propto \frac{eE}{m}\tau\,, \tag{2.12}$$

where τ is the average time between collisions. The collision cross sections for electrons in gas depend strongly on E for most gases. For argon, the elastic cross section goes through a Ramsauer minimum[1] and a maximum, see Fig. 2.2 [Sauli 2023].

Since the average time between collisions τ depends on the electric field through the scattering cross sections, w^- is not linear in E. The mobility of the electrons is therefore found to be a function of the electric field.

[1] Named after C. Ramsauer, who first described that the scattering cross section of electrons in Argon decreases with smaller velocities [Ramsauer 1921].

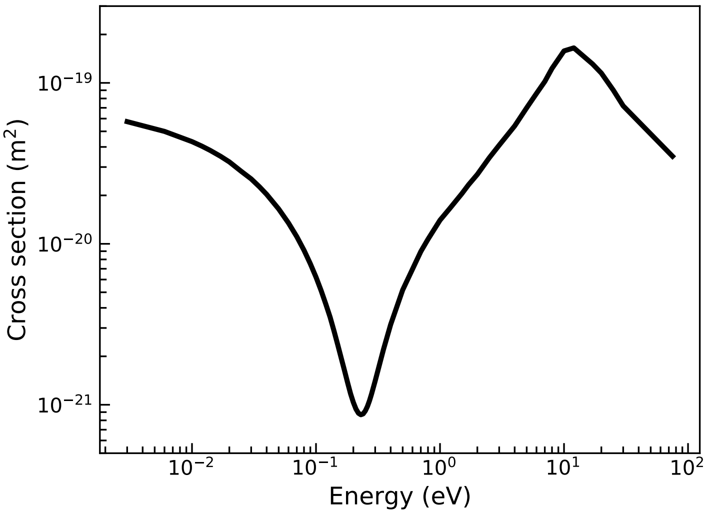

Figure 2.2.: Elastic scattering cross-section for an electron in argon. The scattering cross-section has a clear Ramsauer minimum and a maximum. Data taken from [LXCAT 2023].

For electrons, the drift velocities can be higher than their thermal velocity. This means that the mean energy of the electrons can exceed the thermal energy, and they are no longer in thermal equilibrium with the gas. This affects the diffusion rate, and the factor $k_B T$ in (2.9) has to be replaced by the mean energy ε_k [Leo 1994; Sauli 2023]:

$$\frac{D}{\mu} = \frac{\varepsilon_k}{e} . \tag{2.13}$$

The linear diffusion of the electrons after drifting the distance x is then given by [Sauli 2023]

$$\sigma_x (x) = \sqrt{\frac{2\varepsilon_k}{e} \frac{x}{E}} . \tag{2.14}$$

2.3. Gas Amplification

For very strong electric fields, the process of gas amplification sets in. If the electrons initially created by the ionizing particle, the primary electrons, gain sufficient energy from the electric field within one mean free path length they can themselves ionize gas molecules. This results in about a factor of two more free electrons, the so-called secondary electrons. They in turn also get accelerated by the electric field and subsequently produce tertiary electrons, and so forth. This exponentially increases the number of electrons reaching the readout anode. Since the amount of primary electrons created by the ionizing particle is typically too small to be read out efficiently, this process is usually used to increase the signal height.

The gas amplification can be characterized by the first Townsend coefficient α, which is defined as the inverse of the mean free path of the electron for secondary ionization collisions. If there are n electrons in the beginning, then after a path $\mathrm{d}x$, there will be

$$\mathrm{d}n = n\alpha \mathrm{d}x \tag{2.15}$$

new electrons created. In general, α can be position dependent, as it also depends on the electric field. Integration yields the number of electrons created between positions r_1, r_2 along the path:

$$n = n_0 \exp\left[\int_{r_1}^{r_2} \alpha(x)\,\mathrm{d}x\right] . \tag{2.16}$$

This allows the definition of the gas gain or multiplication factor M, which is defined as

$$M = \frac{n}{n_0} = \exp\left[\int_{r_1}^{r_2} \alpha(x)\,\mathrm{d}x\right] . \tag{2.17}$$

The gas gain is limited to $M < 10^8$. For higher gains, secondary avalanches are formed and breakdown occurs. This is known as the Raether limit.
Due to the higher mobility of the electrons compared to the ions, the avalanche formed in the gas amplification process takes on the form of a liquid drop, as can be seen in Fig. 2.3 [Leo 1994; Sauli 2023].

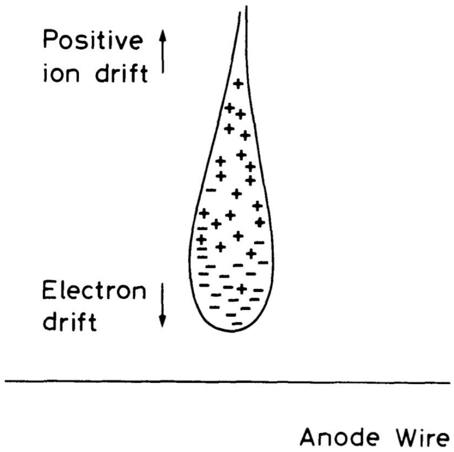

Figure 2.3.: Avalanche formation. Due to the higher mobility of the electrons, the avalanche has the form of a drop, with the electrons in the head and the ions in the tail. Taken from [Leo 1994].

2.4. Cylindrical Gaseous Detectors

This work is focused on cylindrical gaseous detectors. The configuration consists of a container with conducting walls, which are taken to be at ground potential. Along the axis, a thin conducting wire is suspended, which has a positive voltage V_0 applied. The electric field inside the detector is given by

$$E(r) = \frac{1}{r} \frac{V_0}{\ln(b/a)} , \tag{2.18}$$

where a is the wire radius, b the inner radius of the tube and r the radial distance from the axis [Leo 1994]. Note that the electric field increases by $1/r$ toward the wire. This leads to two regions in the detector: Far away from the wire, the moderate electric fields establish a drift region, in which the charges show a drift motion and are not amplified in the gas. If the voltage is high enough, gas amplification can take place near the wire, typically within a few wire radii.

This is called the amplification region. Because of diffusion and the small radius of the anode, after forming the drop shape explained above, the avalanche will surround the wire, see Fig. 2.4. Due to the large difference in mobility, the electrons in the front are collected quickly, while the positive ions drift slowly towards the tube wall. Most of the detected signal is not due to the electron collection but induced by the ion motion away from the anode [Sauli 2023].

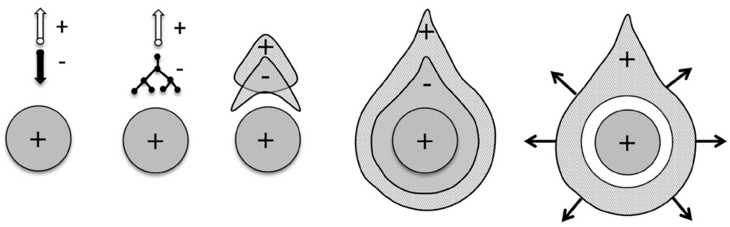

Figure 2.4.: Avalanche formation around a thin wire. Taken from [Sauli 2023].

Fig. 2.5 shows the number of electrons collected as a function of the voltage V_0, which is applied to the anode wire.
At zero voltage, the electron-ion pairs recombine under their own electrical attraction, before they can be collected. As the voltage is raised, the electrical attraction of ions and electrons is overcome, and more and more charge is collected at the electrodes (region I).
At some point, all created pairs will be collected and further increase of the voltage shows no effect, as seen in region II. In this region, the created signal is low and hard to detect. A detector operated in this regime is called ionization chamber.
Further increase of the voltage past region II leads to the onset of gas amplification. Since the electric field is strongest near the anode, this process typically takes place within a few wire radii of the central wire. In this region the gas gain, as defined in Eq. (2.17), is independent of the initial number of electron-ion pairs created. Therefore, the collected charge is directly proportional to the initial number of pairs. A detector operated in this regime is called proportional counter.
This proportionality holds up to point III. If V_0 is increased further, the space charge created by the charge multiplication around the wire becomes sufficiently large that the electric field becomes distorted and the proportionality begins to be lost. This is known as the region of limited proportionality.
Further increase of V_0 leads to the creation of a discharge in the gas. Instead of a single, localized avalanche, many avalanches spread out along the entire length of the anode wire. They are caused by the photons, which are created by recombination of some ions and electrons. They travel to different parts of the detector, where they again ionize the gas and create a secondary avalanche. The output current is therefore completely saturated, independent of the energy of the initial event. Detectors operating in this regime are called Geiger-Müller or breakdown counters. The Geiger-Müller region is characterized by a flat plateau, over which the count rate varies little. The discharge can - apart from a drop in the high voltage applied to the electrodes - only be stopped by the presence of a molecular quenching gas, which can absorb the photons and drain their energy in other channels, without being ionized.
Further increase of the voltage past region IV leads to continuous discharge taking place, independent of whether there is any initially ionizing radiation. This region might be damaging for the detector and is not suited for the detection of particles [Leo 1994].

The detectors discussed in this work are operated in the proportional counter region.

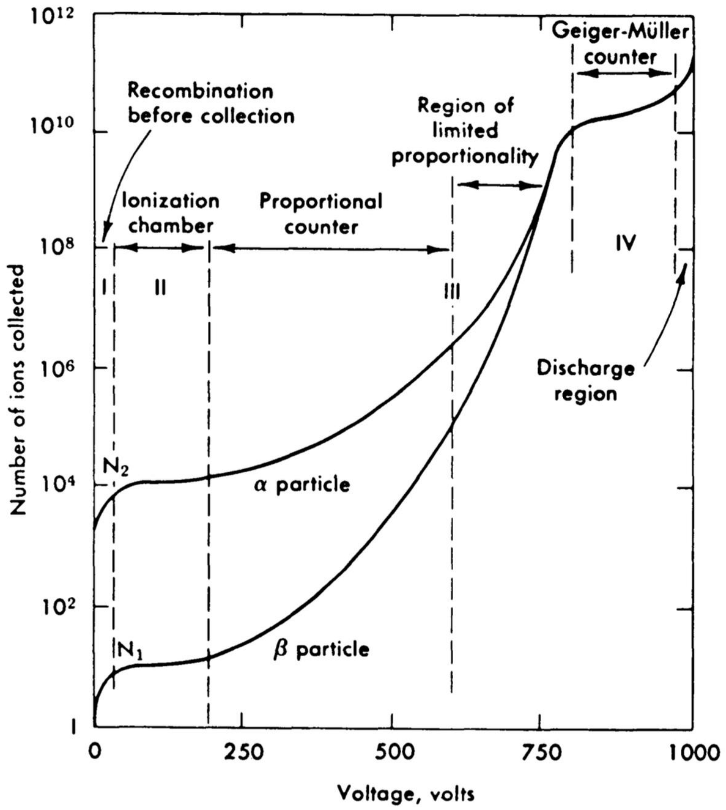

Figure 2.5.: Voltage dependence on the detected charge in a cylindrical gas detector for a highly ionizing α particle, and also a minimally ionizing β. The different operation regimes are explained in the text. Taken from [Melissinos 1966].

3. Monitored Drift Tube (MDT) Chambers

Now that the general physical principles of gaseous detectors have been discussed, we can focus on the specific case of the Monitored Drift Tube (MDT) chambers, as they are used in the ATLAS Muon Spectrometer. A Monitored Drift Tube chamber is a collection of cylindrical gaseous detectors, the so-called drift tubes. It is optically monitored against geometrical deformations such as gravitational sag, hence the name. MDTs are sometimes referred to as Muon Drift Tubes, e.g. in [Arai et al. 2008].

In this chapter, first the structure and the characteristics of a single drift tube are discussed and a brief overview of the structure of MDT chambers is given. In ATLAS, different types of MDT chambers exist. Special emphasis is put on BOS type 3 chambers, as this type is used in the Cosmic Ray Facility. This is followed by a discussion of the signals produced by the detectors, which makes use of a simulation created with Garfield++. Subsequently, the drift time spectrum is introduced as an important quantity for the characterization of MDT performance, and its dependence on the parameters of the gas is considered, also with the help of the Garfield++ simulation. The results will be used in chapter 6 to analyze MDT performance in the Cosmic Ray Facility.

3.1. Mechanical Structure

3.1.1. Single Drift Tube

Firstly, a single drift tube will be considered. The drift tubes are cylindrical gaseous counters and consist of an aluminum tube and an anode wire, which is suspended coaxially at the end of the tube. For the cross-section through a tube, see Fig. 3.1a. In the longitudinal cut in Fig. 3.1b, the suspension mechanism of the wire is illustrated. The Al tube is kept at ground potential and a voltage of 3080 V is applied to the wire.

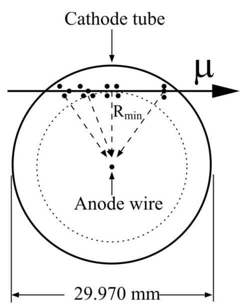

(a) Cross-Section of a single MDT tube. When a muon crosses the volume, the gas is ionized and the electrons drift toward the anode wire. The drift time is a measure for the distance $R_{\min}$ between the muon track and wire.

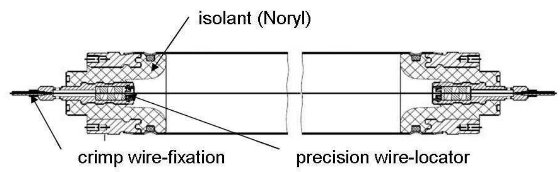

(b) Longitudinal cut through an MDT tube. The wire position is precisely fixed at the ends of the tube and put under suspension. The wire tension is equal to approximately 350 g [ATLAS Muon Collaboration 1997].

Figure 3.1.: Cut views of a drift tube. Pictures taken from [The ATLAS Collaboration 2008].

In ATLAS, the volume inside the tube is filled with Ar/CO_2 in a mixing ratio of 93/7, which is held at an absolute pressure of 3000 mbar. The water admixture is a few hundred ppm: 300 ppm are artificially added to increase the humidity and prevent the formation of cracks in the plastic end plugs of the drift tubes. Typical values are between 300 ppm and 650 ppm H_2O admixture. With the anode voltage of 3080 V, this results in a gas gain is $2 \cdot 10^4$ [Fleischmann 2020; The ATLAS Collaboration 2019].
A single MDT tube has an average spatial resolution of approximately 80 µm [The ATLAS Collaboration 2008]. The characteristics of a single drift tube are summarized in Tab. 3.1.

Table 3.1.: Characteristics of an MDT tube. Adapted from [The ATLAS Collaboration 2008].

Parameter	Design Value
Tube Material	Al
Outer tube diameter	29.970 mm
Tube wall thickness	0.4 mm
Wire Material	gold plated W/Re (97/3)
Wire diameter	50 µm
Gas mixture	Ar/CO_2 (93/7)
Gas pressure	3 bar (absolute)
Gas gain	$2 \cdot 10^4$
Wire potential	3080 V
Maximum drift time	$\sim$ 700 ns
Spatial resolution	$\sim$ 80 µm

3.1.2. Monitored Drift Tube Chamber

An MDT chamber is a collection of up to 432 individual drift tubes. They are arranged in multilayers as shown in Fig. 3.2. The chambers are monitored against geometrical deformations through optical alignment rays.

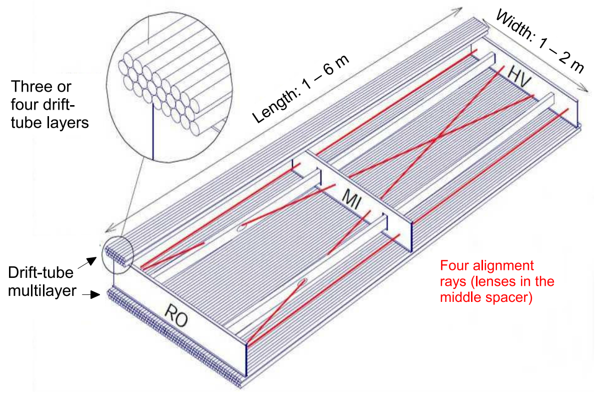

Figure 3.2.: Structure of an MDT chamber. Two multilayers of drift tubes, with three layers each, are mounted on an aluminum spacer frame. Four optical alignment rays monitor the geometry of the chamber for deformations such as gravitational sag. Taken from [The ATLAS Collaboration 2008].

In ATLAS, there are different types of MDT chambers used. They are classified using a three-letter naming scheme, which gives the chamber type and the global location in the ATLAS detector: The first letter describes the region, which can be B (barrel), E (end-caps) or F (forward). The second letter stands for one of four stations, I (inner), M (middle), O (outer) and

E (extra). Finally, the last character distinguishes between L (large) and S (small) sectors. So, for example, an EML chamber is part of the middle layer of a large sector in the end-cap. A BOS chamber is placed in the outer layer of the barrel, in a small sector [ATLAS Muon Collaboration 1997].

For some of the chamber versions, there exist different types.

The Cosmic Ray Facility in Garching contains BOS chambers of type 3. All BOS chambers have two multi-layers with three layers each. The two multi-layers are separated by a 317 mm high spacer structure. The three different kinds of BOS chambers vary in geometry. Tab. 3.2 summarizes the characteristics of BOS type 3.

Table 3.2.: Characteristics of the BOS Type 3 chamber. Adapted from [ATLAS Muon Collaboration 1997].

Parameter	Value
Width	3800 mm
Length	2160 mm
Spacer	317 mm
Thickness	511 mm
Weight	330 kg
No. of layers	2×3
No. of tubes	432

3.2. Detector Signal

MDTs are designed for the detection of muons. If a muon crosses the gas volume, the gas is ionized and the electrons drift toward the anode wire. Once they reach the amplification region, which is within a few wire radii of the anode wire, the gas amplification sets in. The free electrons are picked up by the anode wire, where they can be measured as a charge pulse. See section 2.4.

The signal of the MDTs and the low-level processing by the electronics can be understood with a Garfield++ simulation. Garfield++ is a toolkit for the detailed simulation of particle detectors which are based on the ionization measurement in gases or semiconductors [Schindler 2023a,b; Veenhof 1998]. It has interfaces to various programs which allow detailed simulation of different processes in the detectors. For example, the Magboltz program can be used for the calculation of transport properties of electrons in nearly arbitrary gas mixtures [Biagi and Veenhof 2023], while Heed can simulate the ionization pattern of relativistic charged particles in the detector [Smirnov 2005, 2018]. For the calculation of the electric field, different techniques are available, e.g. the analytical solution in the thin-wire limit and finite element calculations with ANSYS.

Also, the influence of the low-level electronics can be included in the simulation. This is discussed in the following subsection.

3.2.1. Front-End Electronics

The readout electronics are connected to the anode wire through a Hedgehog board, which contains HV decoupling capacitors.
The first step of readout electronics is the Amplifier/Shaper/Discriminator chips, which amplify, shape and discriminate the signal coming from the MDT [Arai et al. 2008]. The electronics will be explained in detail in chapter 4. The response of the amplifier and shaper stages of the ASD

can be modeled using a so-called transfer function, which is defined as the output signal of the electronics in response to a delta peak input. The response to a time-dependent input current $f(t)$ is then given by the convolution of $f(t)$ with the transfer function.

The transfer function used in the simulation, which models the MDT front-end electronics up to, but not including, the Discriminator of the ASD, is shown in Fig. 3.3. It is provided in tabular form on the GitLab repository of Garfield++.[1]

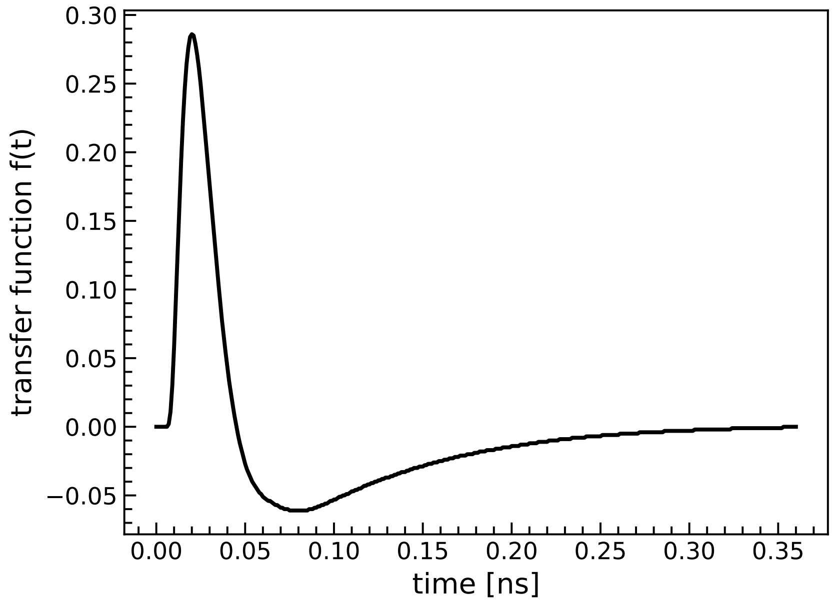

Figure 3.3.: Transfer function used for modeling the analog part of the ASD chip.

The processed signal after convolution with the transfer function is then analyzed by the discriminator part of the ASD, which creates a rectangular pulse. The leading edge of the pulse is the first threshold crossing of the signal, indicating the arrival time of the first $15 - 20$ electrons [Levin et al. 2008] if the threshold is set accordingly. The trailing edge of the rectangular pulse depends on the operation mode of the ASD. This is explained in section 4.4.2.

3.2.2. Garfield++ Simulation

The behavior of single drift tubes is simulated using Garfield++. The simulation explained here is based on a simulation originally developed for Garfield, the predecessor of Garfield++. For the creation of the simulation, also the related example given in [Schindler 2023a] was very helpful.

For the simulation of the drift tubes, the parameters given in Tab. 3.1 were implemented.

In preparation for the drift tube simulation, the table of transport parameters of the gas for different values of E is created using Magboltz. The electric field is calculated using the analytical solutions for the thin wire limit.

The simulation is split into two parts.

[1] `https://gitlab.cern.ch/garfield/garfieldpp/-/tree/master/Examples/DriftTube`

Single Electron

In the first part of the program, the drift and amplification of a single electron is investigated. A single electron is created 1 mm away from the wire. Its drift and the gas amplification near the anode wire are calculated using Runge-Kutta-Fehlberg integration. The integration takes the previously determined transport parameters into account. Also, the drift of the ions created by the gas amplification is calculated [Schindler 2023a]. The drift of the electron and the created ions through the detector are sketched in Fig. 3.4.

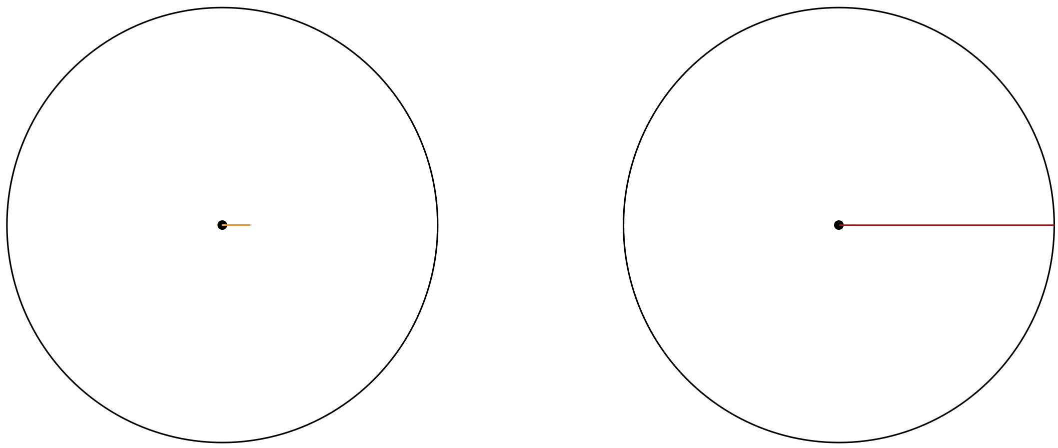

(a) Drift trajectory of a single electron towards the anode wire. For better visibility, the drift distance shown here is twice as long as the one used in the simulation.

(b) Drift trajectory of the created ions away from anode wire.

Figure 3.4.: Drift trajectories for electrons and ions. Initially, a single electron is created at 1 mm distance from the wire. Simulated using Garfiled++.

This process induces a current in the anode wire. It is shown in Fig. 3.5a. The convolution of the current with the transfer function of the electronics is shown in Fig. 3.5b. As a reference for the second part of the simulation, the height of the signal created by a single electron is of interest. Here it is approximately $-0.05\,\mathrm{fC}$.

Muon Event

In the second part, the program simulates muons tracks crossing the tube at a radius R from the center (see Fig. 3.1a). The radius R for this example is set to 75 % of the inner tube radius. The simulated muons have an energy of 4 GeV, as that is the average energy of cosmic muons at ground level given in [Particle Data Group et al. 2022].
The track with drift radius R is given to Heed, which calculates the ionization pattern along the track. In the next step, the drift of the electrons toward the anode wire is calculated using Runge-Kutta-Fehlberg, like in the case of the single electron. The drift lines of the electrons are sketched in Fig. 3.6.

The induced signal is again convoluted with the transfer function: The discriminator part of the ASD is simulated in the sense that the threshold crossing of the signal is recorded. In the simulation, the threshold is set to 15.5 times the amplitude of a single electron signal.

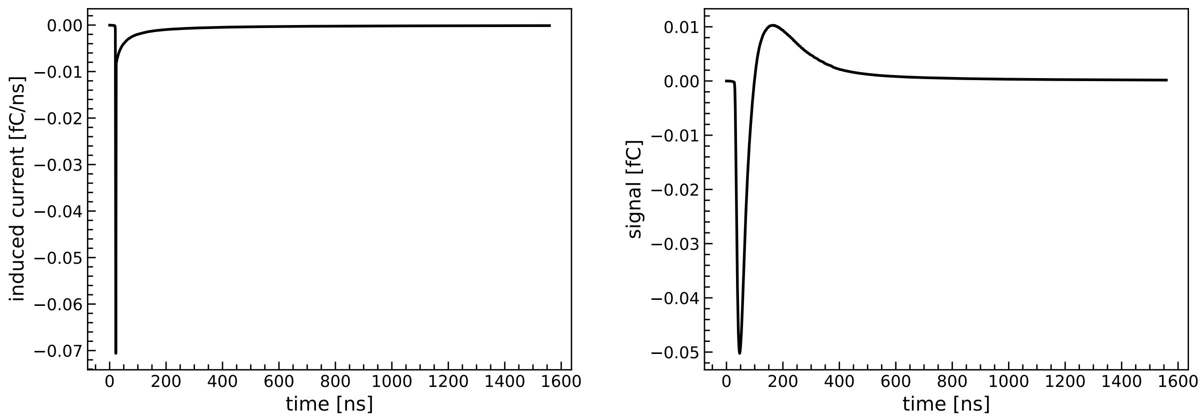

(a) Current induced by the drift and amplification of one primary electron.

(b) Signal after convolution with the transfer function.

Figure 3.5.: Signals produced from a single electron, initially created at 1 mm distance from the anode wire. The bare current is shown in (a), the signal after application of the transfer function in (b).

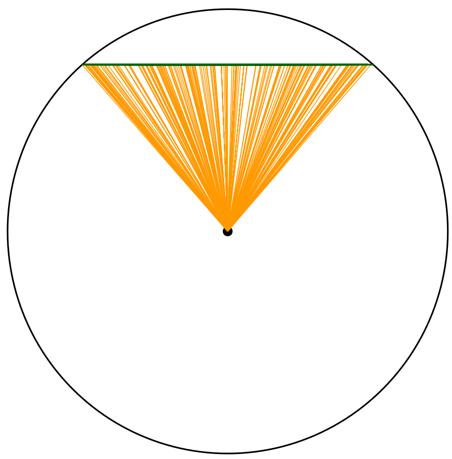

Figure 3.6.: Muon Crossing event in a drift tube. The track of the muon is shown in green. The orange lines are the drift trajectories of the electrons created by the passing muon. The Ion drift lines are not shown here. Created using Garfield++.

3.3. Drift Time Spectrum

3.3.1. Definition

The time between the muon crossing and the arrival of the first $15-20$ electrons determines the drift time. The trajectory of the first electrons corresponds to the particle tracks radial distance R_{min}, as shown in Fig. 3.1a. The drift time is the essential quantity measured in the MDT system. Since the drift time as a function of R_{min} is usually known for the gas composition, it can be used to extract the radius of the particle track.
The primary tool to analyze drift tube performance is the drift time spectrum, which is the histogram of drift times accumulated over many muon crossing events [Levin et al. 2008].

An example of a drift time spectrum of an ATLAS MDT taken during LHC Run 2 is depicted in Fig. 3.7.

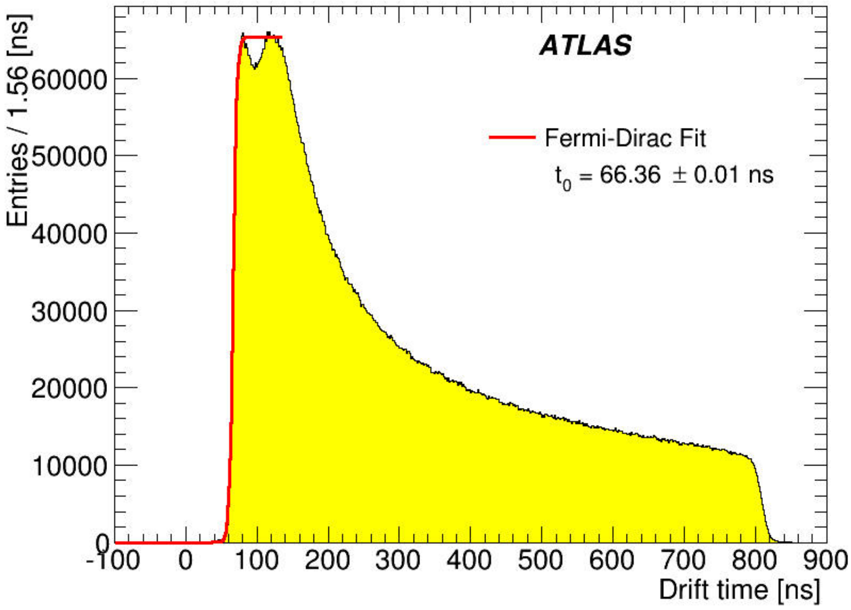

Figure 3.7.: Drift time spectrum of a generic MDT chamber of the ATLAS Muon Spectrometer, accumulated during LHC Run 2. For the calculation of t_0, a Fermi-Dirac fit is made to the leading edge. Taken from [The ATLAS Collaboration 2019].

An important analysis parameter of the drift time spectrum is the maximum drift time t_{max}, since it is very sensitive to the gas composition. It is defined as the time between the half-rise point of the rising edge and the half-fall point of the trailing edge of the drift time spectrum [Levin et al. 2008].

To obtain t_{max} the rising and the trailing edges are fitted with modified Fermi-Dirac functions. The rising edge is fit using

$$f(t) = \frac{A}{1 + \exp\left[(B - t)/C\right]} + k\,, \tag{3.1}$$

while the trailing edge is fit with

$$f(t) = \frac{A + D \cdot t}{1 + \exp\left[(B - t)/C\right]} + k\,, \tag{3.2}$$

where B is the half-rise/half-fall point, C is the rise/fall time and D is the slope at the tail of the distribution. The parameter C changes sign between the rising and the falling edge. A drift time spectrum taken with the legacy readout electronics of the Cosmic Ray Facility with rising and trailing edge fits is shown in Fig. 3.8. Tab. 3.3 lists the corresponding fit parameters. The maximum drift time is then defined as [Levin et al. 2008]

$$t_{\mathrm{max}} = B_{\mathrm{trailing}} - B_{\mathrm{rising}}\,. \tag{3.3}$$

The uncertainty of t_{max} can be estimated from the uncertainties $\Delta B_{\mathrm{rising}}$ and $\Delta B_{\mathrm{falling}}$, which are extracted from the fit:

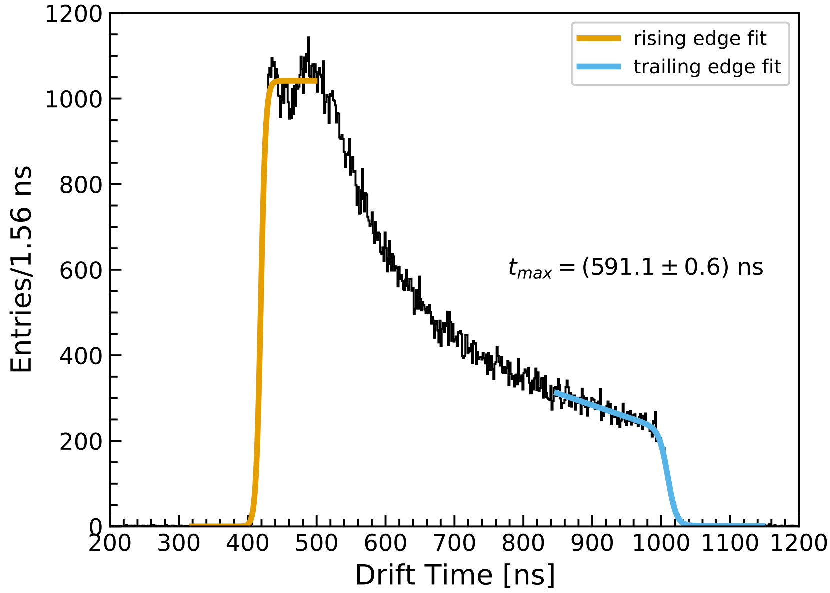

Figure 3.8.: Drift time spectrum measured at the CRF using the legacy readout electronics. Also shown are the rising and trailing edge fits. Tab. 3.3 shows the values of the fit parameters.

Table 3.3.: Rising and trailing edge fit parameters for the measured drift time spectrum shown in Fig. 3.8.

Fit parameter	Value
A_{rising}	1041 ± 7
B_{rising}	(418.96 ± 0.18) ns
C_{rising}	(3.48 ± 0.16) ns
k_{rising}	0 ± 4

Fit parameter	Value
$A_{trailing}$	780 ± 30
$B_{trailing}$	(1010.0 ± 0.5) ns
$C_{trailing}$	(-6.3 ± 0.5) ns
$D_{trailing}$	(-0.55 ± 0.04) ns^{-1}
$k_{trailing}$	1.4 ± 1.5

$$\Delta t_{\max} = \sqrt{\Delta B_{\text{trailing}}^2 + \Delta B_{\text{rising}}^2}\,. \tag{3.4}$$

For the fit in Fig. 3.8, the maximum drift time is $t_{\max} = (591.1 \pm 0.6)$ ns.

Along with the maximum drift time, also the half rise time $t_0 := B_{\text{rising}}$ is used in chapter 5 to verify the functionality of the upgraded MDT readout system of the Cosmic Ray Facility.

3.3.2. Drift Time Spectrum from Garfield++

In the program, the drift time measurement is achieved by finding the first crossing of the detector signal over the level of 15.5 times the amplitude of a single electron signal. By repeating the simulation 10^5 times, with sampling of the drift radius R from a uniform distribution, the drift time spectrum is accumulated.

The drift time spectrum obtained with this simulation for the default conditions inside an MDT is shown in Fig. 3.9. The maximum drift time of (722.8 ± 0.3) ns agrees well with the values given in [Levin et al. 2008].

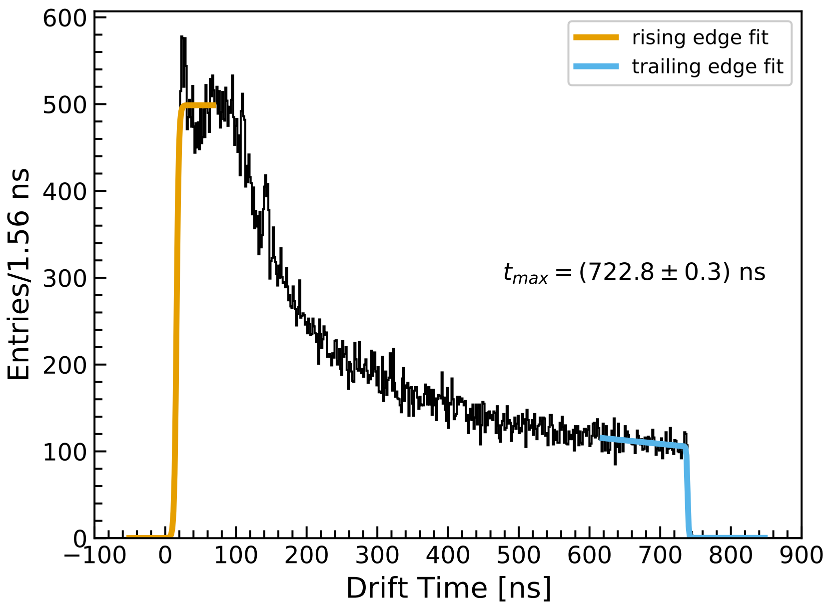

Figure 3.9.: Drift time spectrum obtained with the Garfield++ simulation. The gas mixture for this simulation was Ar/CO_2 in the ratio 93/7.

3.3.3. Dependence of the Drift Time Spectrum on the Gas (Garfield++)

In [Levin et al. 2008], the influence of different gas parameters on the maximum drift time $t_{\max}$ is investigated using Garfield simulations. In the simulations, the pressure, temperature, H_2O content and the Ar/CO_2 mixing ratio of the gas were varied, and linear $t_{\max}$ dependencies on the parameters obtained. From this, the Ar/CO_2 mixing ratio was determined to have the biggest possible influence on the maximum drift time, based on the expected uncertainties of the parameters in our setup. In [Levin et al. 2008] the maximum drift time as a function of CO_2 content is approximated with a linear dependence given by $-89\,\text{ns/Vol\%}$. This is obtained with CO_2 contents beween 6.7 Vol% and 7.3 Vol%.

The temperature dependence was investigated in [Engl 2007], but is not further considered here, because the Cosmic Ray Facility is operated in a temperature-stabilized measuring hall.

The Garfield++ simulation was used to investigate the Ar/CO_2 mixing ratio dependence of the drift time spectrum and consequently of $t_{\max}$. It also provides a reference for the analysis of the MDT behavior in the Cosmic Ray Facility. Systematic experimental studies on the $t_{\max}$ dependence on the CO_2 fraction were also done in [Tyler 2011] and are used as a source of validation for the simulation.

The mixing ratio is varied in steps of one percent, from 92/8 to 97/3. The resulting drift time spectra are fit using eq. (3.1) and (3.2) to determine the maximum drift time. The dependence of the maximum drift time on the CO_2 content and a selection of the simulated drift time spectra are shown in Fig. 3.10. The $t_{\max}$ values are compared to the measurements from [Tyler 2011]. In the simulation, the gain was fixed to 2×10^4. The same was achieved in the measurement by adjusting the voltage [Tyler 2011]. Simulation and measurement are found to be in good agreement.

In chapter 6, the $t_{\max}$ dependence shown in Fig. 3.10b will be used to determine the CO_2 content of the gas used in the Cosmic Ray Facility.

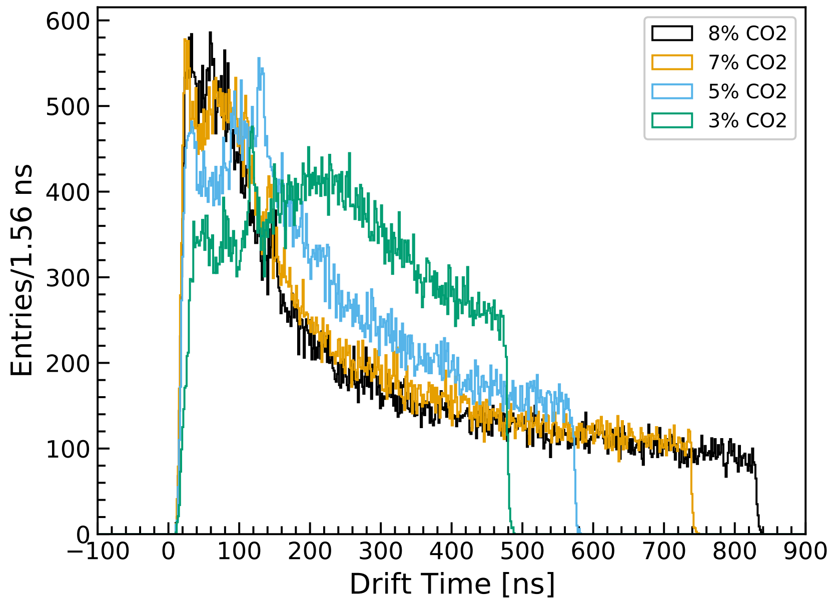

(a) Drift time spectra for different CO_2 contents. With higher CO_2 content the drift time spectrum gets longer and the relative height of the first peak increases.

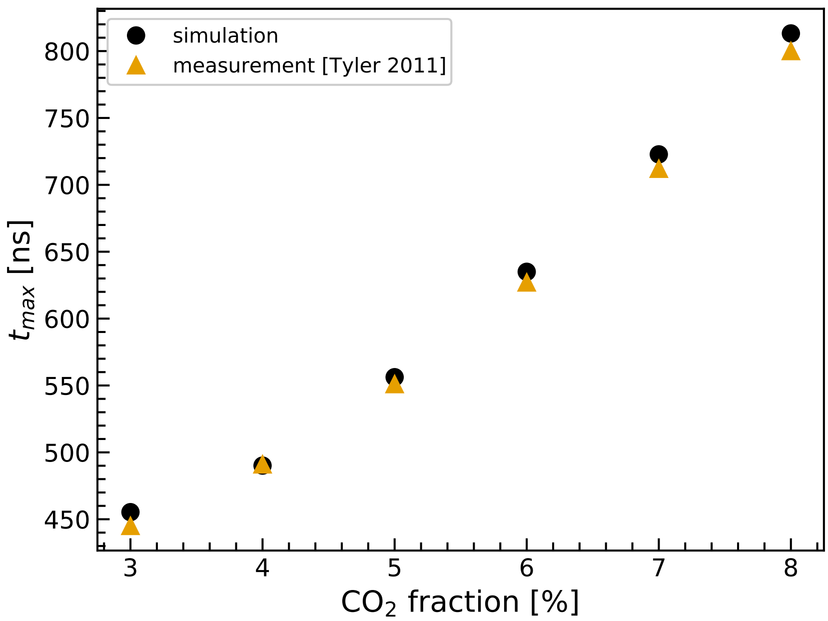

(b) $t_{\max}$ as a function of CO_2 content. The simulation is compared with the measurement results from [Tyler 2011]. They are in good agreement.

Figure 3.10.: The dependence of the drift time spectrum on the Ar/CO_2 mixing ratio.

4. MDT Electronics

In this chapter, the readout system of the ATLAS MDT electronics will be explained. There are multiple versions of the MDT electronics: development versions before the installation in ATLAS, the version that is currently installed in the ATLAS Muon Spectrometer, and lastly the Phase-II electronics that were developed in preparation for High Luminosity LHC.

We focus here on the version of the MDT electronics, as it is presently installed in ATLAS. The differences between the development system used in the Cosmic Ray Facility, and its upgrade to the present ATLAS MDT electronics, will be discussed in chapter 5. In the outlook of chapter 7, a brief overview of the Phase-II electronics will be given.

4.1. Overview

An overview of the data flow in the present MDT front-end electronics is shown in Fig. 4.1. The individual components are explained in the following sections.

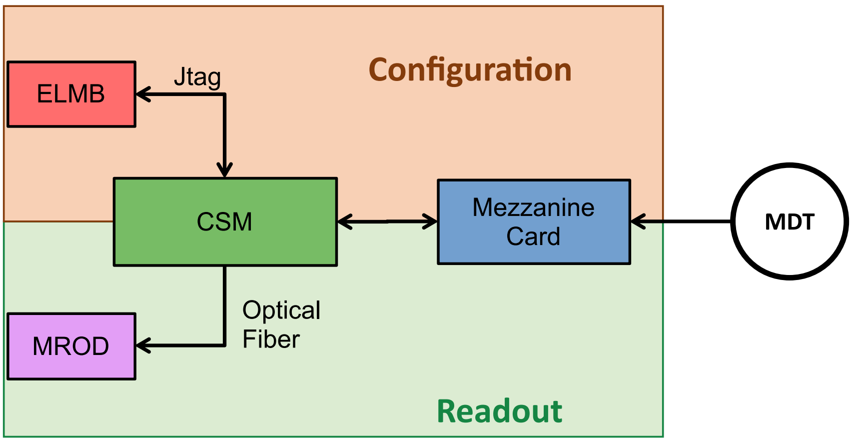

Figure 4.1.: Flowchart of the current MDT electronics. Not shown are the hedgehog boards, which interface the mezzanine boards with the tubes and decouple the electronics from the high voltage. Adapted from [The ATLAS Collaboration 2017].

The signals from 24 drift tubes are interfaced to one mezzanine card through a hedgehog board, which decouples the electronics from the high voltage. The signals are processed and digitized by the mezzanine card, which sends the data to the Chamber Service Module (CSM). The CSM multiplexes the data it receives from up to 18 Mezzanine Cards and sends it to the Muon Read Out Driver (MROD). A single MROD can receive data from up to six CSMs. The Chamber Service Module and the Mezzanine Cards are configured via the Embedded Local Monitor Board (ELMB), using the JTAG protocol. The data taking is steered by the Timing, Trigger and Control (TTC) system, which sends triggers, timing information and event identifiers to the CSM, which distributes the information to the mezzanine cards [Arai et al. 2008]. The on-chamber electronics are shown in Fig. 4.2.

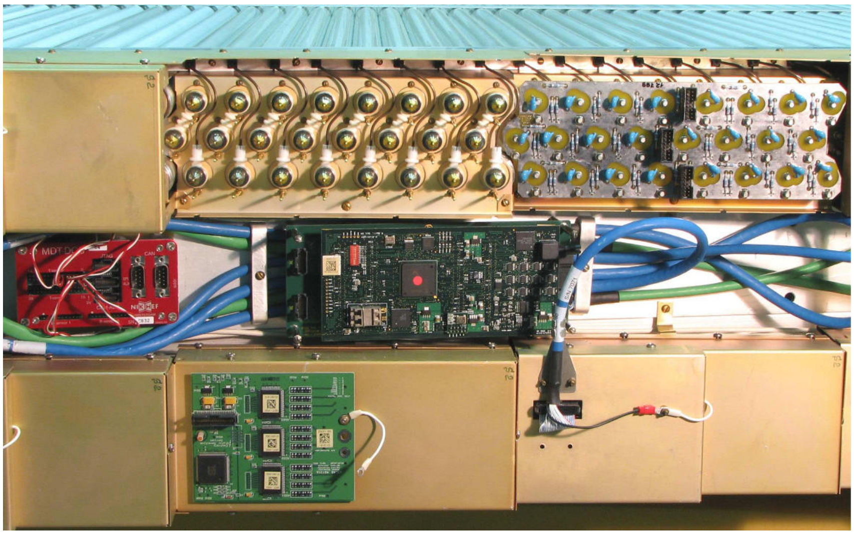

Figure 4.2.: Photograph of the MDT electronics needed for the readout of the chamber. The assembly has been staged in sections to illustrate the components. One hedgehog board is attached to the tube ends (upper right), one mezzanine board is visible and not plugged in (lower left), while a second one which is connected to the CSM motherboard is completely enclosed by its aluminum Faraday cage in the lower right. In the center, the CSM can be seen. The red box on the left is the MDT-DCS, containing an embedded local monitor board (ELMB). Taken from [Arai et al. 2008].

In the following, first the configuration of the electronics is explained. Then, an overview of the trigger system will be given. Finally, the readout electronics will be explained, in the order that the data travels from the anode to the back-end electronics.

4.2. Configuration

For the configuration of the MDT front-end electronics, ATLAS uses the MDT Detector Control System (MDT-DCS) module. It is based on the Embedded Local Monitor Board (ELMB), a general-purpose plug-on board that was developed by the ATLAS collaboration to serve various detector control tasks. It is not specific to the MDT control system and is also used in other parts of the ATLAS detector and outside the ATLAS experiment at CERN [Boterenbrood 2011].

There is one MDT-DCS module on each ATLAS MDT chamber. The programmable parameters of the front-end electronics are sent to the module via the Controller Area Network (CAN) bus, using the CANopen protocol. The MDT-DCS sends the parameters via JTAG to the CSM, and through the CSM to the mezzanine boards. Additionally, there are 7 Digital I/Os for control output to the CSM and error status readout from the CSM. The MDT-DCS module is shown in Fig 4.3.
The MDT-DCS also monitors the environmental parameters of the chamber, that is the temperature and the magnetic field, as well as the temperatures and voltages of the CSM and mezzanine cards [Boterenbrood 2011].

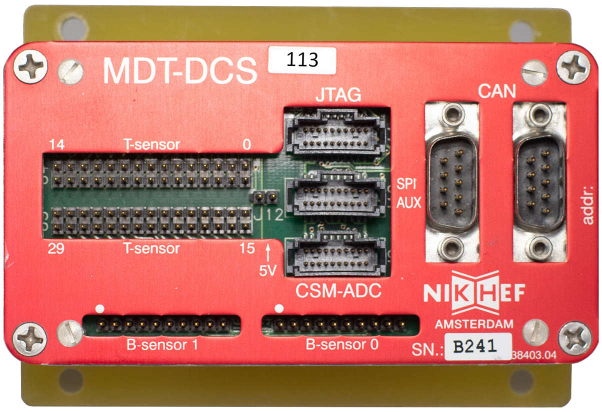

Figure 4.3.: Picture of the MDT-DCS Module. The connectors on the left, which are labeled with T-sensor, are for the temperature sensors of the chamber, and the ones on the bottom are for the magnetic field sensors. In the middle are three connectors: The upper one is the JTAG interface for CSM configuration, the lower one is the SPI interface to the ADC on the CSM, while the middle connector is a spare digital interface. On the right-hand side, there are two CAN connectors. The sticker in the upper middle (113) is the CAN Node Address of the module [Boterenbrood 2011].

4.3. Trigger and Timing

The readout electronics needs a reference for the time measurements. The distribution is achieved with the Timing, Trigger and Control (TTC) system. It is used not only in the ATLAS experiment but also in other experiments at CERN.

The time measurements are performed in units of the TTC clock of 40.08 MHz, which is the bunch crossing frequency at LHC. The time given by the TTC clock is referred to as "coarse time" or bunch crossing ID (BCID) and is stored in a 12-bit word [Arai et al. 2008].

The Timing, Trigger and Control system provides for the distribution of synchronous timing, trigger and control signals to the different detector systems. If the TTC system receives a trigger accept signal, it creates the event identifier (EVID) and triggers the readout electronics.

The TTC system provides different modules for operation. There exists the TTC-VMEbus Interface, the TTCvi, which connects the TTC to the trigger processor.
The TTC signal is transmitted with TTC Laser transmitters, of which exist different versions, some of which can supply up to 448 destinations. There is a low-power version, called the TTCvx, which is meant for system integration and prototyping and can supply 4 destinations.
The TTCrx receiver ASIC can decode the TTC optical signals.

For the MDT readout electronics, a TTC laser transmitter sends timing and trigger information to the CSM, which decodes it with a TTCrx receiver. The CSM then distributes the TTC information to the 18 connected mezzanine cards, which perform the time measurements.

More information on the TTC can be found on [Baron 2021].

4.4. Readout Electronics

In this section, the readout electronics required for data acquisition with an MDT chamber are explained. The order of the explanation follows the data path: from the decoupling electronics attached to the anode wire, via the mezzanine board and the CSM to the back-end Muon Readout Driver.

4.4.1. Hedgehog Board

The signal hedgehog board is a front-end interconnection board. It decouples the readout electronics from the high voltage applied to the anode wire. For a photograph of a hedgehog board, see Fig. 4.4. Different hedgehog cards exist to accommodate for differing MDT chamber geometries. One hedgehog board services 24 drift tubes [Arai et al. 2008].

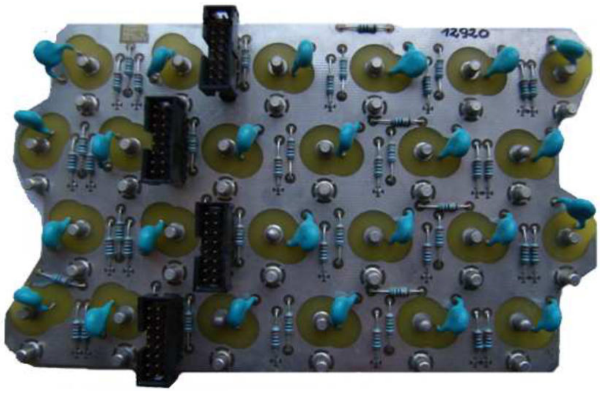

Figure 4.4.: Photograph of a hedgehog board. The mezzanine board can be connected via the black connectors. The board shown in the picture is designed for a chamber that has four tube layers. The 4-layer boards have 6 channels per layer and the 3-layer boards have 8 channels per layer. Both versions have a total of 24 layers. Taken from [Arai et al. 2008].

In addition to the HV protection by the 470 pF capacitor on the hedgehog board, overcurrent input protection circuitry is placed on the mezzanine card itself, see BAV99 in Fig. 4.5. A circuit diagram of the complete input connection circuitry of a single mezzanine card channel is shown in Fig. 4.5.

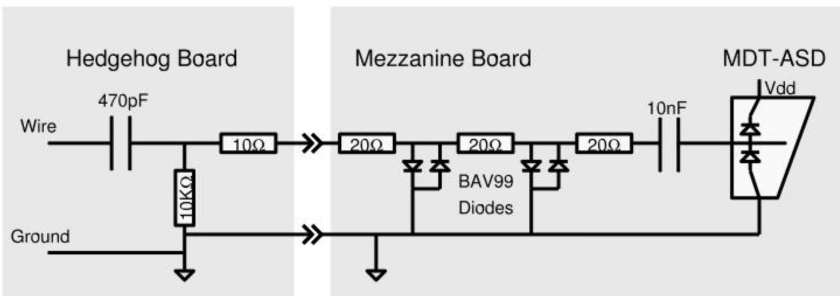

Figure 4.5.: Input protection for a single channel of the mezzanine board. The circuitry of the one channel on the hedgehog board is shown on the left. Taken from [Arai et al. 2008].

4.4.2. Mezzanine Cards

The mezzanine boards carry the lowest level of active readout electronics. The signals of the tubes are passed to the Amplifier/Shaper/Discriminator (ASD) chips in groups of eight. There are three ASD chips on each mezzanine board, which can read out 24 tubes. The ASD chips pass the signal on to a single Time-to-Digital (TDC) chip with 24 channels, the Atlas Muon TDC version 3 (AMT-3). Two different mezzanine card types exist, depending on whether a chamber has three or four layers of tubes [Arai 2003]. A mezzanine card for a 3-layer chamber is shown in Fig. 4.6.

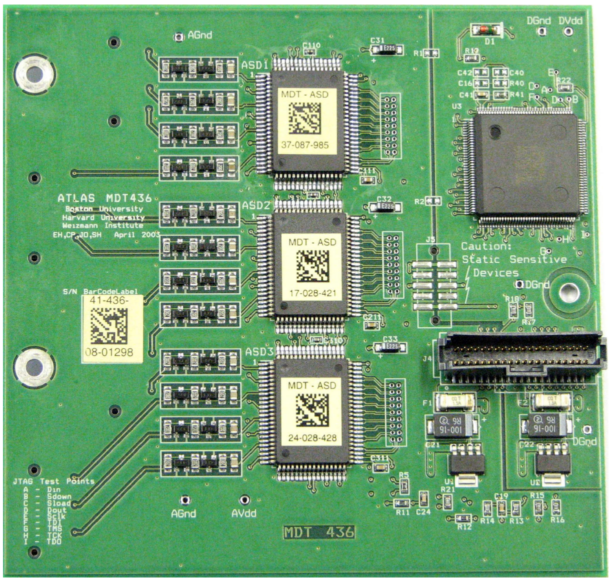

Figure 4.6.: Picture of a Mezzanine Card for a chamber with three tube layers. In the middle of the board, the three ASD chips are placed. The black chip in the upper right is the AMT-3 and below it is the CSM cable connector. The input protection circuitry is on the left. Taken from [Arai et al. 2008].

The output of the ASDs is a rectangular pulse, with the leading edge encoding the threshold crossing time of the signal pulse and the trailing edge encoding either the signal charge integrated in a given time window or the time over threshold of the signal, depending on the mode of operation [Posch, Hazen, and Oliver 2007].

The TDC performs the time measurements of the 24 channel inputs from the ASD chips. The time tags of the leading and trailing edges are encoded using 17 bits. The first 12 bits are the coarse time, which records the time in 24.95 ns steps of the TTC clock. The last 5 bits encode the fine time with $\frac{24.95}{32}\,\text{ns} \approx 0.78\,\text{ns}$ resolution. The TDC receives the TTC information from the CSM [Arai et al. 2008].

Additionally, trigger matching between the trigger time tag and the time measurements is performed by the TDC. The event data is encoded in 32 bit words and consists of an event header, the data words of the event and finally an event trailer. The different 32 bit word formats sent by the TDC are explained in [Arai 2003]. As an example, the word formats for the TDC event header, event trailer and the time measurement of a leading or trailing edge are shown in Fig. 4.7. The accepted event data is stored in an output buffer [Arai et al. 2008].

The TDC ID used in the data words has four bits, i.e. it can take only 16 values. One Chamber Service Module, which is discussed in the next section, can take up to 18 Mezzanine cards. The TDC ID is therefore not enough to distinguish between the 18 cards. This apparent conundrum has a solution, as will be explained in the following.

TDC header: Event header from TDC

31	30	29	28	27	26	25	24	23	22	21	20	19	18	17	16	15	14	13	12	11	10	9	8	7	6	5	4	3	2	1	0
1	0	1	0	TDC ID				Event ID												Bunch ID											

TDC: Programmed ID of TDC.
Event ID: Event ID from event counter.
Bunch ID: Bunch ID of trigger (trigger time tag).

TDC trailer: Event trailer from TDC

31	30	29	28	27	26	25	24	23	22	21	20	19	18	17	16	15	14	13	12	11	10	9	8	7	6	5	4	3	2	1	0
1	1	0	0	TDC ID				Event ID												Word Count											

Word count: Number of words from TDC (incl. headers and trailers).

Single measurement data: Single edge time measurement

31	30	29	28	27	26	25	24	23	22	21	20	19	18	17	16	15	14	13	12	11	10	9	8	7	6	5	4	3	2	1	0
0	0	1	1	TDC ID				Channel					T	E	Coarse Time												Fine Time				

Channel: TDC channel number.
Coarse Time: Coarse time measurement (in bins of 25ns).
Fine Time: Fine time measurement from PLL (in bins of 25ns/32).
T: Edge type: 1 = leading edge, 0 = trailing edge.
E: Error. An error has been detected in the hit measurement (a coarse counter error, a channel select error, or a rejected hit error)

Figure 4.7.: The TDC words, TDC header, TDC trailer and single measurement data. The first four bits are the identifier of the word type. The four bits after that are the TDC ID. In the case of the single measurement data, a five-bit channel number follows. The four-bit TDC ID can only take 16 different values, even though there are 18 Mezzanine cards connected to one CSM. Adapted from [Arai 2003].

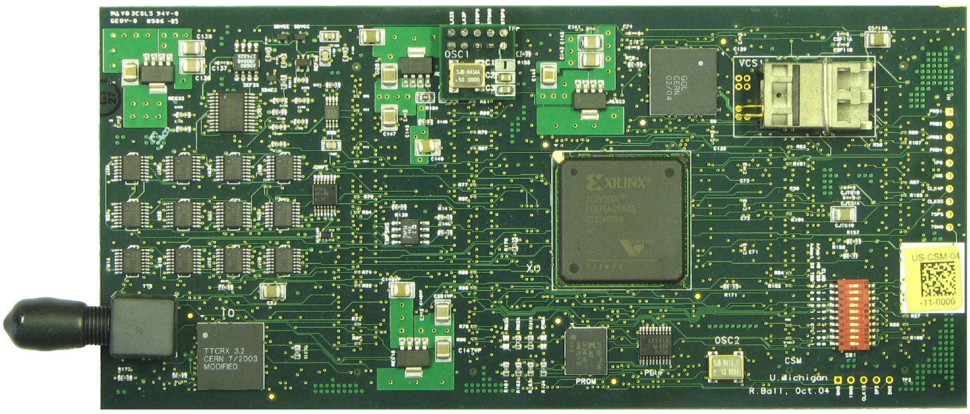

Figure 4.8.: Picture of a Chamber Service Module. In the lower-left corner, the TTCrx optical receiver for the TTC signal is placed. On the upper edge in the middle, the add-on board for 50 MHz operation is soldered on. It is labeled as OSC1. In the middle of the board is the FPGA which takes care of the multiplexing. Finally, in the upper right corner, is the optical transceiver for communication with the readout electronics, in the case of the ATLAS setup the MROD. Taken from [Arai et al. 2008].

4.4.3. Chamber Service Module (CSM)

The Mezzanine Cards are read out by the Chamber Service Modules (CSMs). One CSM can be connected to up to 18 Mezzanine Cards. This is done via a passive interconnection board, the CSM Motherboard, shown in Fig. 4.9. The CSM Motherboard also provides the connectors for JTAG and the CSM-ADC, as well as the power connector.

The CSM is the central piece of electronics in the MDT readout chain. It has several functions:

it receives the TTC signals via its TTCrx receiver and delivers them to all connected mezzanine boards. Further, it receives the data from the mezzanine boards and creates a single output stream. It sends the output stream to the MROD via a gigabit optical link (GOL). In addition, it provides voltage and temperature information to the ELMB and routes JTAG signals from the ELMB to the TDC chips on the mezzanine boards. The TDC controls the parameters of the ASD chips through its interface logic [Arai et al. 2008].

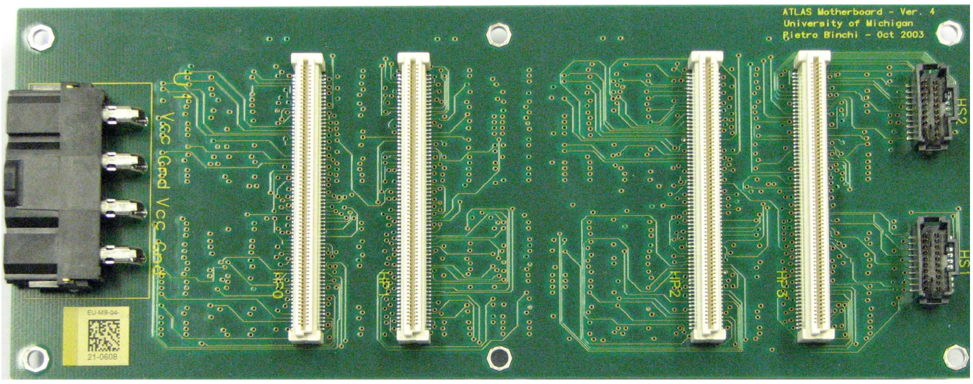

(a) Top

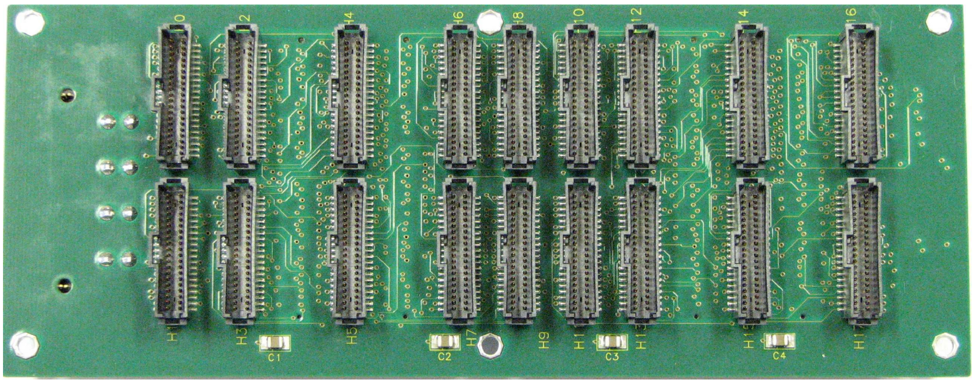

(b) Bottom

Figure 4.9.: CSM Motherboard. The top side, shown in (a), has four white connectors into which the CSM is plugged in. On the right-hand side, the two connectors for JTAG and CSM-ADC can be seen, and on the left of the board, the power connector is placed. The bottom is shown in (b). Here the 18 connectors for the Mezzanine Cards are placed.

To create the single output stream from the 18 TDC inputs, the present MDT readout system is run in the time-multiplexing mode of the CSM. The CSM polls for data from each of the 18 TDCs in turn. If data from the TDC is present, it is put into the output stream, if no data is present, an empty word is sent. The TDC number of the data is then determined by the timing position in the data stream. This solves the problem of the TDC ID only taking 16 different values. For synchronization, spacer words are sent between the last TDC word of the current and the first TDC word of the next cycle [Chapman et al. 2007]. The time multiplexing scheme is illustrated in Fig. 4.10.

The CSM has two operation speeds: it is possible to choose between 25 MHz 32 bit word rate and 50 MHz 32 bit word rate. For operation at the higher speed, an add-on board containing a 50 MHz crystal oscillator was added to the CSM modules [Arai et al. 2008]. The CSM modules were originally produced without this add-on board and were only capable of stable operation at 25 MHz. A photograph of a CSM with add-on board is shown in Fig. 4.8.

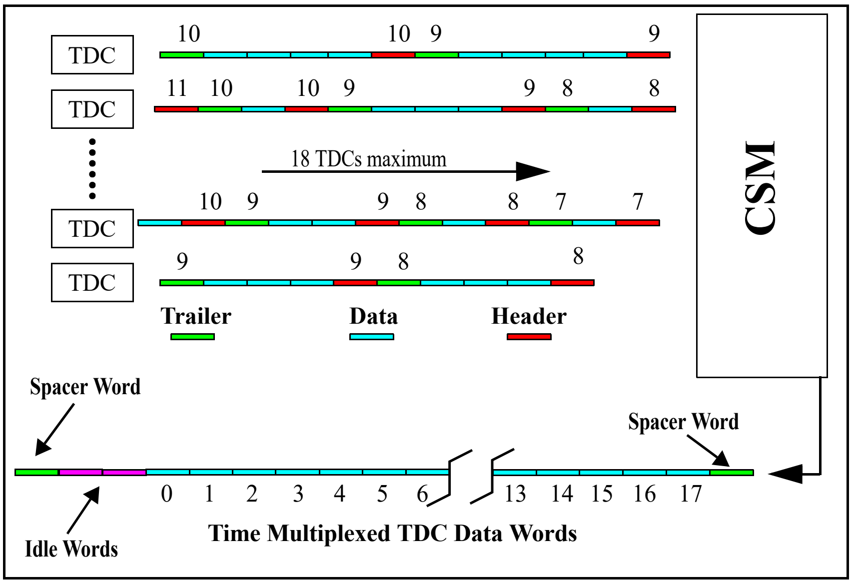

Figure 4.10.: The time multiplexing implemented in the current MDT readout. The TDCs send data words enclosed by headers and trailers. For example, TDC 0 has the complete events 9 and 10 in its output buffer and TDC 1 has the complete events 8, 9 and 10 as well as the header for event 11 in its output buffer. The CSM reads 32-bit words from the individual TDCs in turn, in fixed order. If the TDC provides a data word, it is put in the output stream. If not, an empty word is sent instead. For synchronization with the MROD, the CSM sends a spacer word and two idle words after every round of TDC polling. Taken from [Chapman et al. 2007].

4.4.4. MDT Read Out Driver (MROD)

The Chamber Service Module sends its output stream to the MDT Read Out Driver (MROD). One MROD can read out up to 6 CSM cards, as can be seen in Fig. 4.11. It receives event data from the CSMs via optical link, builds event fragments at a maximum rate of 100 kHz and outputs these to the ATLAS data-acquisition system. It also takes care of monitoring and error checking as well as handling and flagging of the data [Boterenbrood et al. 2006].

Since the MROD modules are getting old and there are only ~ 10 spare modules left, an alternative backup was developed: the FELIX-MROD. It is based on the Front End Link eXchange (FELIX) card, that was originally developed for the HL-LHC upgrades of ATLAS. It has become now an independent trigger and data acquisition project. With different firmware, the FELIX card can act as a FELIX-MROD. The FELIX-MROD alone does not yet perform any event-building. This is done with an additional step, the Software Read Out Driver (SW ROD) [ATLAS FELIX Group 2023; König 2020]. The FELIX Card FLX-712 is shown in Fig. 4.12.

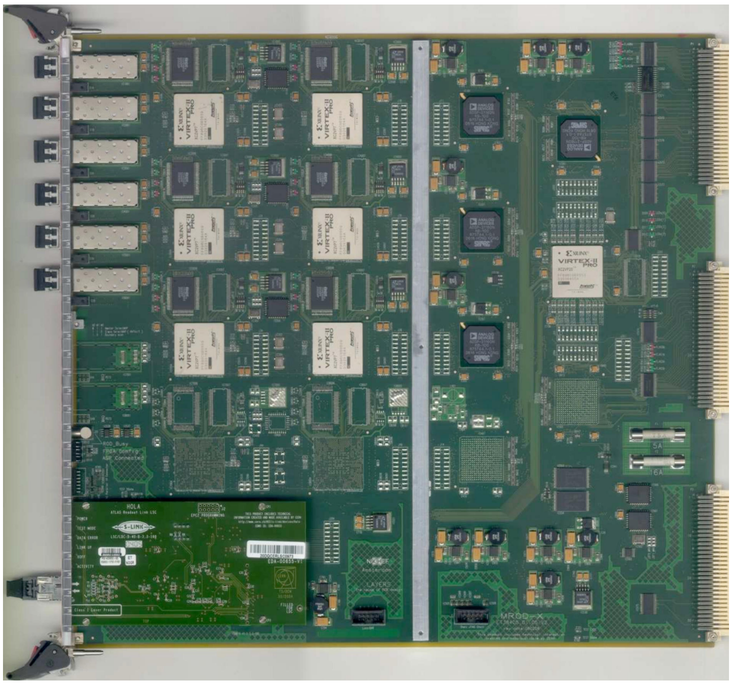

Figure 4.11.: The MROD board: In the upper left are six optical fiber connectors. One CSM can be connected to each of them. The metallic square integrated circuits are FPGAs, 6 of them in the upper left handle the input from the CSMs. The FPGA in the middle right is the MROD output FPGA. The S-link daughter card in the lower left is the connection for the Read-Out Link. Taken from [Arai et al. 2008].

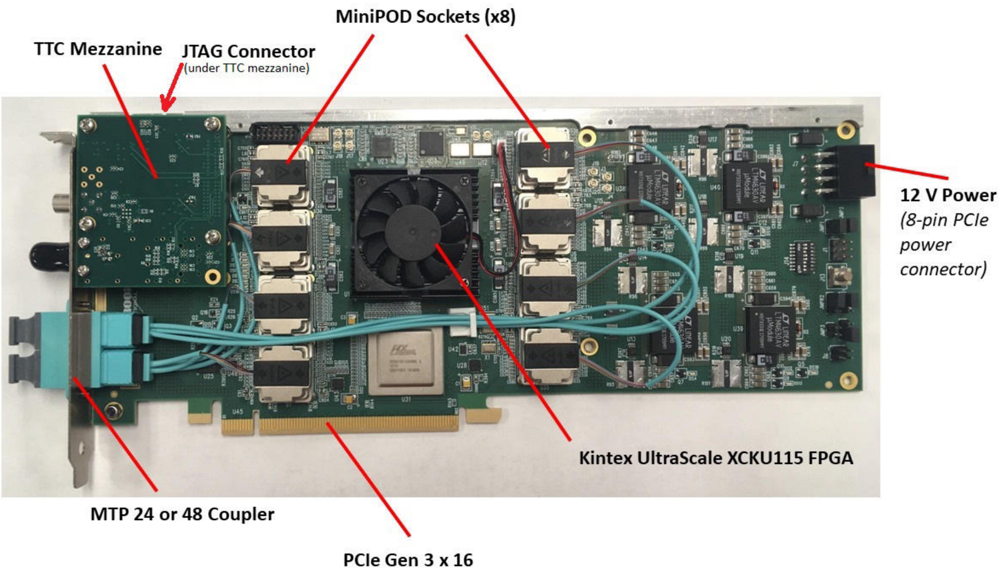

Figure 4.12.: The FLX-712 card. The red arrows indicate the most important features. With alternate firmware, the FLX-712 can substitute an MROD. Taken from [ATLAS FELIX Group 2023].

5. Upgrade of the Garching Cosmic Ray Facility

In this chapter, the upgrade process of the Cosmic Ray Facility (CRF) in Garching is described. The upgrade is necessary for the CRF to be compatible with the current ATLAS standard and to prepare for tests of Phase-II ATLAS MDT electronics.

First, a general overview of the CRF is provided. Then the legacy readout electronics and the differences to the ATLAS standard are explained. This is followed by the presentation of the upgrade process. Finally, the steps necessary for backward compatibility with the legacy readout system are discussed.

5.1. Setup of the Cosmic Ray Facility

The Cosmic Ray Facility (CRF) is a detector system in Garching that is used to detect cosmic muons. It consists of two MDT chambers of BOS type for precision tracking of the muons as well as two sets of scintillators, one on top and one on the bottom of the setup. The sets of scintillators are referred to as hodoscopes and are used for triggering the readout system. The setup is shown in Fig. 5.1.

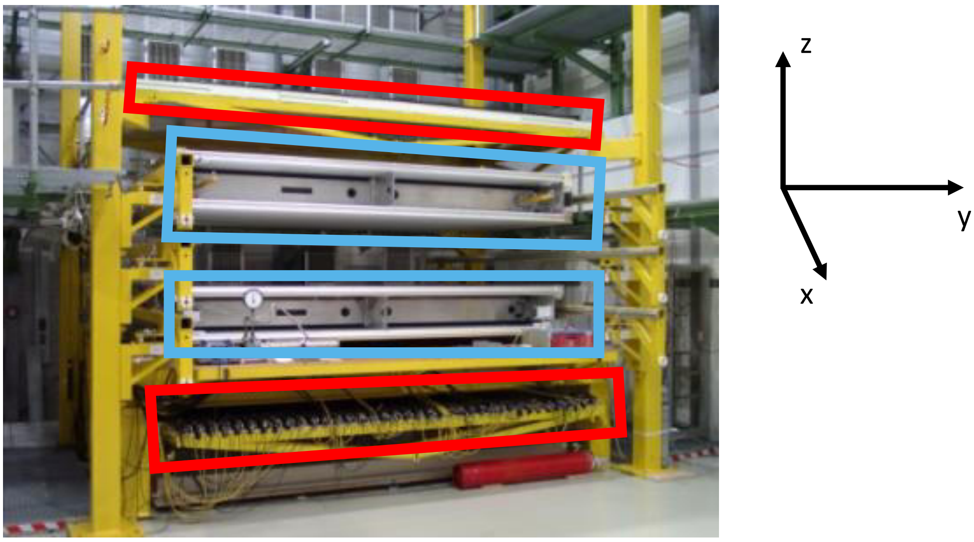

Figure 5.1.: Picture of the Garching Cosmic Ray Facility. Shown in blue are the two MDT Chambers of BOS type. The positions of the hodoscopes are indicated in red. The photomultipliers of the lower hodoscope are clearly visible. The scintillators of the upper hodoscope are hidden behind the structure. Between the two MDT chambers is a slot for a third chamber to be inserted. For reference a Cartesian coordinate system is defined: the x-axis is taken to be perpendicular to the MDT tubes, the y-axis is parallel to the MDTs. Adapted from [LMU Munich 2023].

The detector sub-systems are read out by different readout lines: The MDTs are read by legacy MDT front-end electronics, which need to be upgraded to the present ATLAS standard. The data of the hodoscopes is analyzed by modules in a VME crate. If the upper and lower hodoscopes are hit in coincidence, a TTCvx module sends out a trigger to the CSMs.

Different analysis scripts are in place that merge and analyze the data from the different readout lines.

The setup allows for the construction of reference tracks: The x-coordinates, as defined in 5.1, can be determined with BOS MDT chambers to $\sim 80\,\mu\text{m}$ precision [The ATLAS Collaboration 2008], while the y-coordinate has a resolution of 10 cm, given by the width of the scintillators. These reference tracks can then be used to test and calibrate a BOS or Micromegas detector, which can be inserted in the slot between the two MDT chambers.

This has been used e.g. in [Herrmann 2019] for testing and precision calibration of Micromegas modules for the ATLAS New Small Wheel.

5.2. Legacy Readout Electronics

A flowchart of the legacy system is shown in Fig. 5.2.

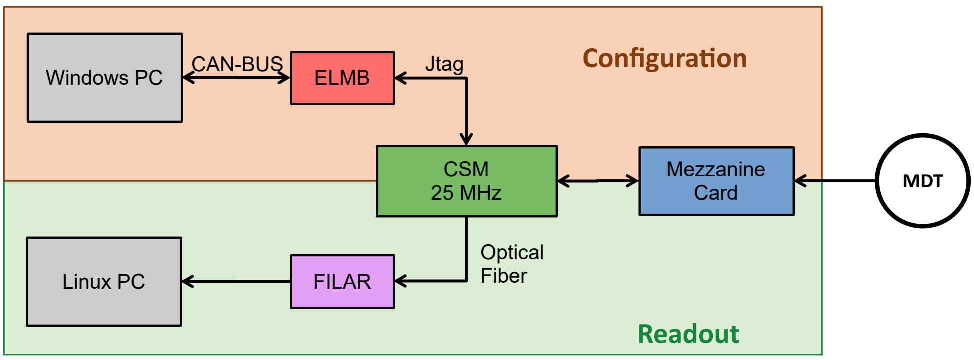

Figure 5.2.: Flowchart of the legacy CRF electronics. Note that the CSM operates at 25 MHz readout speed and does not have the 50 MHz oscillator add-on board installed. Furthermore, the system is read out by a FILAR card instead of an MROD.

There are two main differences to the readout electronics presently used in ATLAS: firstly, the CSM does not send the data to an MROD but instead to a FILAR card, and secondly, the CSM does not have the 50 MHz add-on board and is operated at 25 MHz. The FILAR card is shown in Fig. 5.3. The CSM without 50 MHz-oscillator add-on is compared to the version currently used in ATLAS in Fig. 5.4.

The CSM in the legacy setup, apart from the lower operation frequency, also used a different method to create the combined data stream from the 18 TDC inputs: the so-called event-builder mode. The original design of the CSM included this as a legacy mode for compatibility with an earlier version of the CSM, the CSM-0. Unlike in the setup of the present MDT electronics in ATLAS, the CSM does not time-multiplex the data from the TDCs into 18 different time slots, but it does the event building itself. It collects the data words from the TDCs of a specific event ID (EVID) and constructs a CSM event from it. The CSM event uses a similar format as the TDC events that are sent to the CSM: first, a CSM header containing the EVID and the bunch crossing ID (BCID) is sent, followed by all the data words, and is concluded by the CSM event trailer, which contains the word count of the event block. After the event is written to the output buffer, the CSM begins the assembly of the next event [Ball et al. 2004]. In the legacy readout

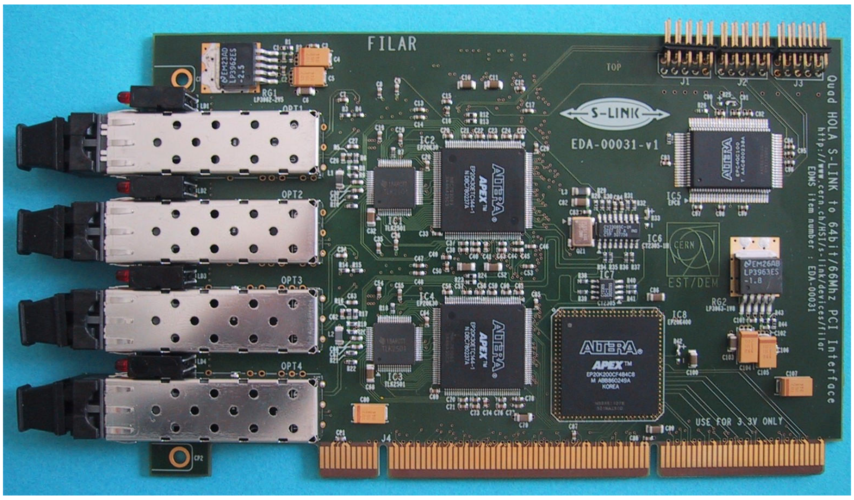

Figure 5.3.: Photograph of the FILAR card. Taken from [Haas 2005].

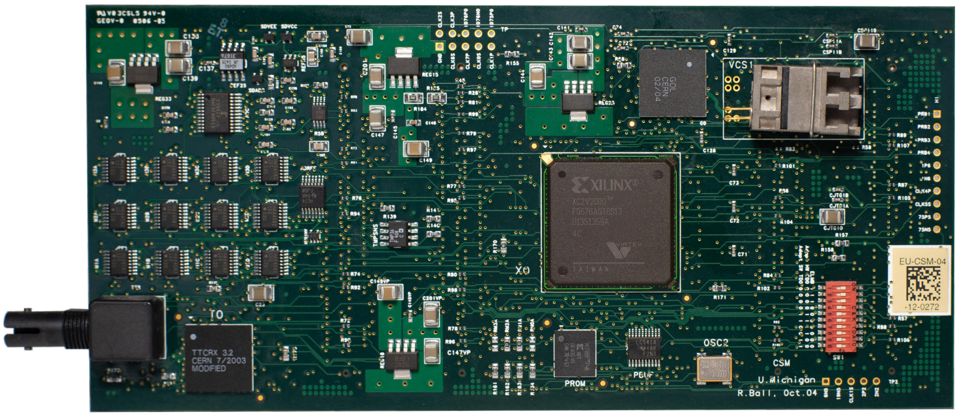

(a) CSM without 50 MHz oscillator.

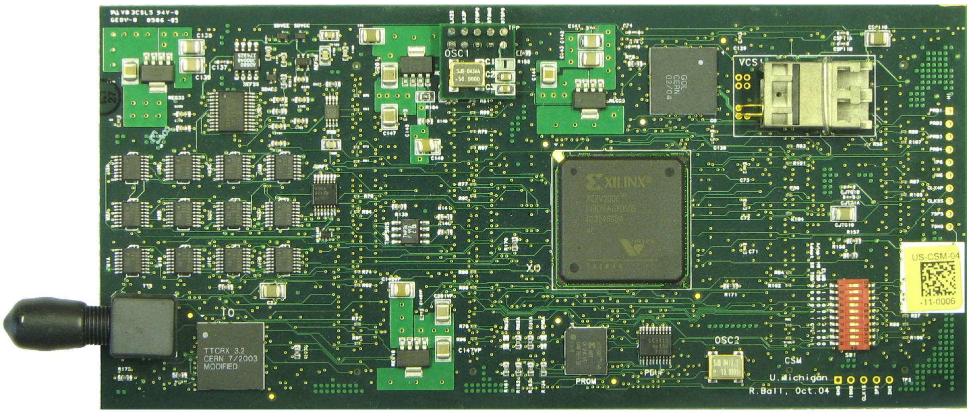

(b) CSM with 50 MHz oscillator. Taken from [Arai et al. 2008]

Figure 5.4.: Comparison of the legacy CSM used in the CRF (a) and the upgraded version used in ATLAS (b).

system of the CRF, the CSM headers and trailers are replaced by separator words containing the event ID and the word count before each event. The event-builder mode is illustrated in Fig. 5.5.

The attentive reader will have noticed that in event-builder mode, the problem of the TDC ID (see section 4.4.2) has not yet been addressed. It is solved in a different way than in the

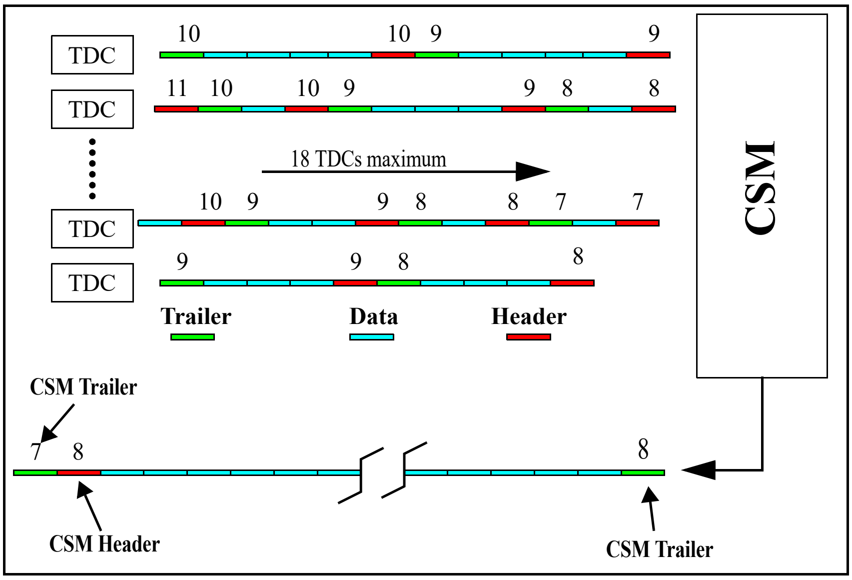

Figure 5.5.: The CSM-0 legacy mode, which is also available in the original CSM-4 design. The CSM takes over the event building. It orders the data from the TDCs by EVID. First, a CSM Header is sent, followed by the TDC data words belonging to the event and finally the CSM trailer. For an explanation of the illustration of the TDC data, see Fig. 4.10. In the legacy readout system of the CRF, the CSM headers and trailers are replaced by a single separator word containing the event ID and the word count before each event. Taken from [Ball et al. 2004].

time-multiplexing mode. The four-bit TDC ID is not enough to encode 18 TDCs. However, the channel has five bits, which is more than needed to encode the 24 channels. The trick is to combine the TDC ID and the channel to form the wire number, with a total of nine bits. This can be seen in Fig. 5.6. A nine-bit field - corresponding to 512 possible values - is enough to encode the $18 \cdot 24 = 432$ wire numbers. Therefore a mapping between the mezzanine card channels and the wire number is made [Ball et al. 2004].

<table>
<tr><td>31</td><td>30</td><td>29</td><td>28</td><td>27</td><td>26</td><td>25</td><td>24</td><td>23</td><td>22</td><td>21</td><td>20</td><td>19</td><td>18</td><td>17</td><td>16</td><td>15</td><td>14</td><td>13</td><td>12</td><td>11</td><td>10</td><td>9</td><td>8</td><td>7</td><td>6</td><td>5</td><td>4</td><td>3</td><td>2</td><td>1</td><td>0</td></tr>
<tr><td>0</td><td>0</td><td>1</td><td>1</td><td colspan="4">TDC ID</td><td colspan="5">Channel</td><td>T</td><td>E</td><td colspan="12">Coarse Time</td><td colspan="5">Fine Time</td></tr>
</table>

(a) The AMT-3 format.

0011	Wire Number	T	E	Coarse Time	Fine Time

(b) Single measurement word in wire number format.

Figure 5.6.: The two formats for a single TDC measurement data word, side by side. The AMT-3 format (a) is taken from [Arai 2003], while (b) is taken from [Ball et al. 2004]. The original AMT-3 word has separate TDC ID and channel fields, while the format created in event builder mode combines them to form a 9 bit wire number.

In the case of the original CSM-0 design, this mapping is as follows: TDCs 0-15 with channels 0-23 are mapped to TDC IDs 0-15 with channel IDs 0-23. TDC 16 is mapped to TDC 0, 1, 2 with channels 24-31. TDC 17 is mapped to TDC ID 4, 5, 6 with channel IDs 24-31 [Ball et al. 2004]. It turns out that the mapping in the Cosmic Ray Facility is slightly different: TDC 17 is mapped to TDC ID 3, 4, 5 channel IDs 24-31, the remaining mapping rules are the same.

The FILAR card does not have event-building capabilities and only stores the data received from the CSMs to the disk. One file is created for each CSM that is being read out. Also, an additional file is created for the data from the VME crate, that records the data from the hodoscope.

A variety of analysis scripts exists on the readout system which allow the merging and the analysis of the recorded data. They combine the data from the same event from the different sub-systems and analyze the combined data. They apply various corrections and analyses and produce the reference tracks that have been used for testing and commissioning of detectors for ATLAS, see e.g. [Herrmann 2019].

Part of those analysis scripts is the jitter correction. The electronics which are used in the CRF were designed for use in ATLAS, which works on a base frequency of 40 MHz since that is the rate with which bunches of protons are colliding in the detector region. Therefore, the trigger electronics can only send out triggers every 25 ns, at the ticks of the bunch clock. This is designed for use in ATLAS, but the cosmic muons detected in the CRF do not adhere to this bunching of events. Thus an artificial jitter of up to 25 ns is introduced by the trigger system. However, by measuring the time between the trigger created by the scintillators and the next bunch clock cycle, at which the trigger is emitted to the CSM, this can be corrected. This is illustrated in Fig. 5.7.

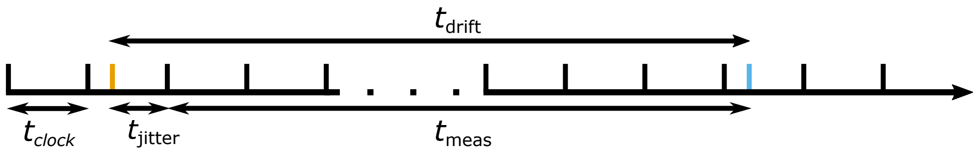

Figure 5.7.: Illustration of the jitter introduced by the cosmic muons not adhering to the 40 MHz bunch clock. The bunch clock cycles are shown in black and repeat every $t_{\text{clock}} =$ 25 ns. The time of the hodoscope trigger is shown in orange, the time to the next bunch clock cycle is t_{jitter}. The MDT system measures the time t_{meas} from the next bunch clock cycle after the muon click to the threshold crossing of the signal in the MDT, here shown in blue. Since the maximum drift time in the MDT is $t_{\text{max}} \approx 600$ ns, this can be up to ~ 24 bunch clock cycles later. To correct for the jitter, t_{jitter} has to be measured and added to t_{meas} for each event individually, to obtain the true drift time t_{drift} .

It is therefore clear that after the upgrade to the present ATLAS MDT electronics, it is desirable to keep backward compatibility with the existing analysis routines. This would allow the use the Cosmic Ray Facility for the same purposes as before, without the need to rewrite all the analysis programs.

5.3. Electronics Upgrade

The readout electronics of the CRF shall be upgraded to the present ATLAS standard.

So, to upgrade the system to the present MDT electronics, the FILAR card has to be exchanged to MROD and the CSM card has to be upgraded to the version with the 50 MHz-oscillator add-on. Since the MRODs are not available, the upgrade will use FELIX-MROD, which was developed as an alternative.

Note that it is not possible to start with a partial upgrade, where FELIX-MROD is used in combination with a legacy CSM, which does not have the add-on board. The FELIX optical transceivers are at the low end of their working range when operating at 50 MHz 32-bit word rate, and do not have the option to be operated at 25 MHz. As an alternative, it would be possible to change the firmware of the legacy CSM for operation at 50 MHz. This was tried when the communication frequency of the CSMs had to be doubled in ATLAS, but the result did not prove to be stable.[1]

To establish compatibility with FELIX-MROD, it is therefore necessary to replace the Chamber Service Module with the version with the add-on board installed. The upgrade to the 50 MHz CSM does not require any physical changes on the Mezzanine cards: The legacy CSM just needs to be removed from the Motherboard, and the new CSM be plugged in. The Mezzanine cards are intrinsically compatible with operation at double readout speed.

However, significant changes needed to be done to the configuration setup. It was necessary to upgrade the firmware on the MDT-DCS box. This was done with the `ELMBLoader` program and the correct firmware, which were both provided by H. Boterenbrood. Also, a program that creates the configuration bit stream and sends it to the ELMB was provided by him. There, some modifications had to be made, since the original program loads the parameters from a CERN database. It has been modified to load the parameter from text files, which allows more convenient changing of parameters. The final adapted source code for the programming of the CSM and Mezzanine cards of the upgraded Cosmic Ray Facility is referred to as `csm-configurator`.[2]

The `csm-configurator` is command line based and is designed for operation on Linux machines. This allows the elimination of the Windows PC from the upgraded setup since it was used only for the configuration of the legacy electronics. The flowchart of the resulting readout system is depicted in Fig. 5.8.

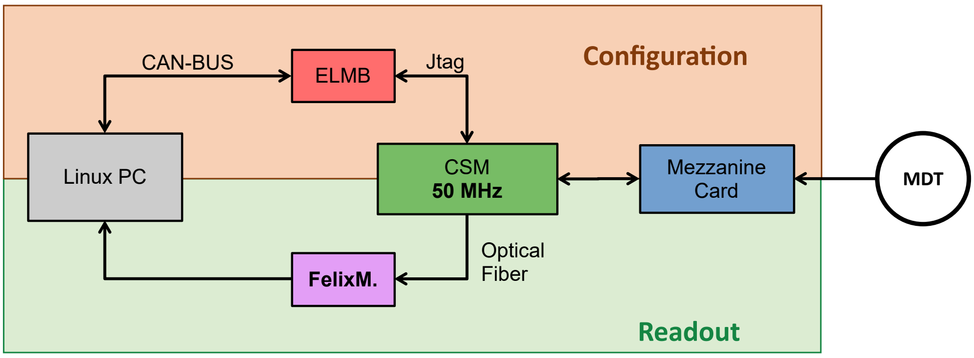

Figure 5.8.: Flowchart of the new CRF electronics. The working principle is the same as in Fig. 5.2. For compatibility with the current MDT readout electronics in ATLAS, the FILAR card was replaced by FELIX-MROD (FelixM.). Due to incompatibility of FELIX-MROD with the 25 MHz CSM, it had to be replaced by a 50 MHz CSM, which required updating of the ELMB firmware and new configuration software. This allowed us to install the configuration program on the same Linux PC that is used for readout.

An introduction on how to use the FELIX-MROD based system for recording data is given in appendix B.

5.4. Compatibility to the Legacy Readout System

As argued in section 5.2, it is desirable to reuse the existing analysis routines that provide jitter correction, track reconstruction and many additional functionalities.

[1] T. Wijnen, private communication.

[2] Source code available on `https://gitlab.physik.uni-muenchen.de/crf-upgrade/csm-configurator`.

To ensure this compatibility, the most obvious course of action is to transform the data recorded by FELIX-MROD to a format that is identical to the one produced by FILAR. Then, the analysis scripts can be called on files of the same format as the ones produced by the legacy setup.

To achieve this, one has to understand the differences in the recorded data. Let us analyze this in a top-down approach. The uppermost level of the stored data is the data container format saved by FELIX-MROD and FILAR. The CSM sends binary data to the readout module, which saves it to file, surrounded by a header and trailer structure. For FELIX-MROD this structure is quite complex and explained in [ATLAS FELIX Group 2023]. The main idea is sketched in Fig. 5.9

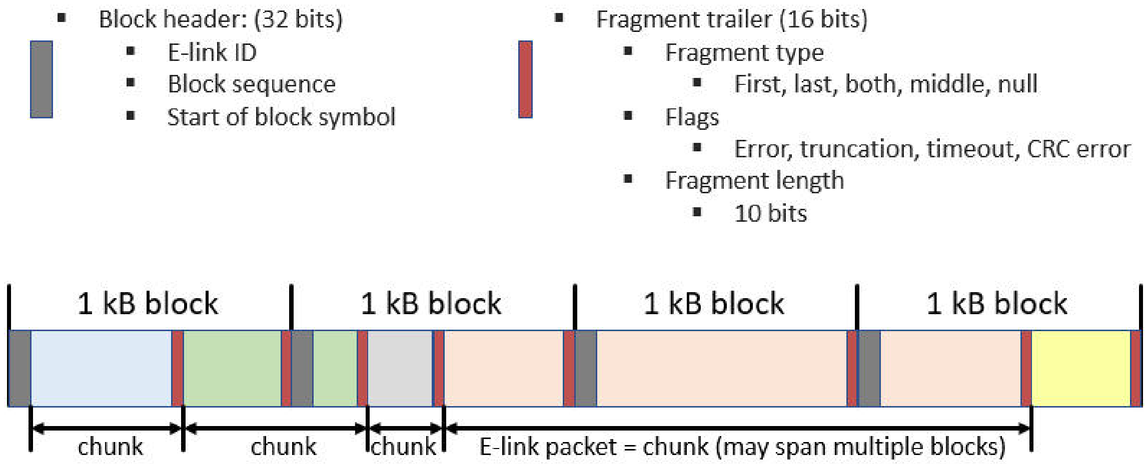

Figure 5.9.: Block structure used in the files stored by FELIX. The data is structured in 1 kB blocks, which contain data from a specific source. The source is specified in the block header. Inside the block, there can be more than one chunk of data, which are separated by fragment trailers, which contain error information and fragment length. It can occur that the available space in the 1 kB block is not enough to save a chunk. As a consequence, chunks can be split into fragments. Information about the fragment type (first, last, middle, both) is also saved in the fragment trailer. Taken from [ATLAS FELIX Group 2023].

The structure produced by FILAR is rather simple: It is based on 32 bit words, like the CSM and TDC data words. It is structured in blocks, that start with 11 32 bit words, that contain information about the stored data. The first and the last word of the header contain information about the length of the following data block. This is the only information relevant to the analysis scripts. After the header, the data words sent by the CSM are stored.

Independent of the use of FILAR or FELIX-MROD, the way the CSM assembles the data words is different. As explained before, the present ATLAS MDT CSM works in time-multiplexing mode, where the basic structure is as follows: first, a spacer word is sent, then two idle words for synchronization, see Fig. 5.10a. This is followed by 18 TDC words, one from each TDC read out by the CSM in fixed order. Then, the next spacer word is sent and so on. The legacy CSM, on the other hand, uses the event-builder mode explained in section 5.2. It assembles the TDC data words from the TDCs into event blocks, separated by separator words containing the event ID and the word count before each event, see Fig. 5.5. For overview, the figures describing the two readout modes are repeated side by side in Fig. 5.10.

It has to be noted, that the event building mode was disregarded, as in ATLAS the event building takes place at a later stage, namely the MRODs. Firmware that would allow operation in event builder mode is not available for the 50 MHz CSMs.

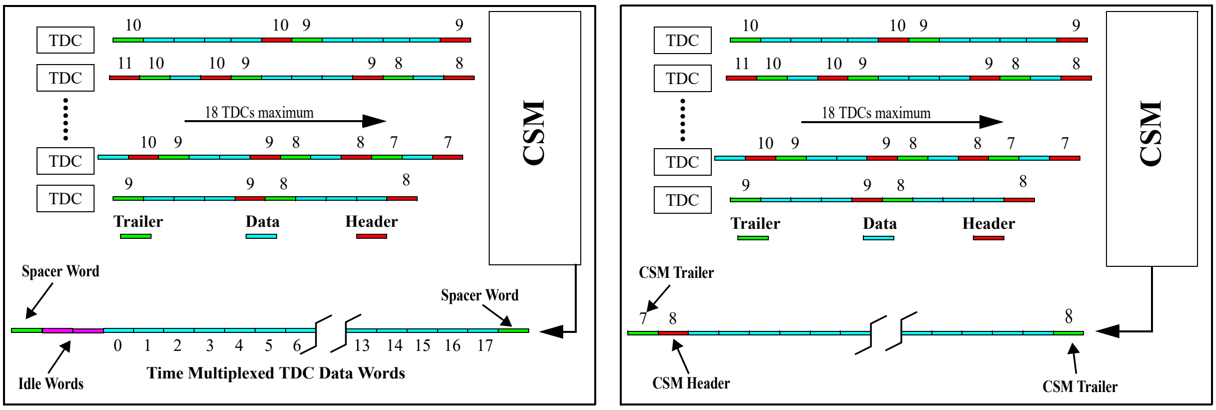

(a) The time multiplexing mode. Taken from [Chapman et al. 2007].

(b) The event building mode. In the legacy readout system of the CRF, the CSM headers and trailers are replaced by a single separator word containing the event ID and the word count before each event. Taken from [Ball et al. 2004].

Figure 5.10.: The two readout modes of the CSM, side by side. The updated CSMs use the time-multiplexing mode shown in (a). The CSM does not perform event building, but only multiplexes the data from the TDCs into the output stream. The legacy CSM uses the event-building mode: It orders the TDC data by event ID and produces CSM separator words before each event block. The TDC headers and trailers are disregarded. This is shown in (b).

Finally, the differences in the 32 bit words have to be investigated. The TDC header and trailer words are not recorded by the FILAR system in Garching. They are replaced in function by the CSM headers and trailers. Also, as mentioned before, the TDC ID problem is solved differently by the two setups. The result is, that in the legacy setup the so-called wire number is used, while in the present ATLAS readout electronics, the unaltered AMT-3 format introduced in section 4.4.2 finds application. Examples of single measurement words for both formats are shown in Fig. 5.6.

With those differences in the format understood, the `MDTEventBuilder`[3] program was written to convert the data files produced by FELIX-MROD into the FILAR format.

To do this, the program first gets the raw CSM data from the "chunks" in the FELIX-MROD data file. The CSM data is saved in the multiplexing format. The program splits the multiplexed data into one input stream per TDC and assembles the events by EVID. In the process, it maps the TDC and channel to the wire number and replaces the according bits in the data word. If all 18 TDCs have sent the event trailer to the event, a CSM separator word in the format of the legacy system is created and written to an output buffer, together with the reformatted data words of the TDCs. After a certain number of events, a FILAR header is created and the block of CSM data is written to file. The product is a file in the FILAR format, which can be analyzed by the analysis programs.

Note that if the file produced by the `MDTEventBuilder` program is to be used with the analysis scripts, the corresponding VME file of the legacy readout has to be altered: in the configuration of the legacy readout, the chambers to be read out are set. This information is recorded in the header of the VME file as a colon-separated list. Since the FELIX-MROD file is not produced by the legacy readout, the converted file has to be added manually to that list.

[3]Source code available on `https://gitlab.physik.uni-muenchen.de/crf-upgrade/mdteventbuilder`.

The correct function of the upgraded readout and `MDTEventBuilder` is verified in the following chapter.

6. Results

In this chapter the performance of the Upgrade is analyzed, using data taken with the legacy and the FELIX-MROD setup simultaneously and comparing the two. The upper reference MDT chamber was read out with the legacy FILAR setup and the lower one with the FELIX-MROD based setup. The data were taken with the same configuration of the Mezzanine cards and the CSMs for both setups.

First, the raw data of the two setups are compared. Afterward, the performance of the analysis scripts is investigated. In the last section of this chapter, a discrepancy between the drift time spectra taken with the CRF and the expected spectra with ATLAS gas parameters is investigated.

6.1. Comparison of the Legacy and the Upgraded Readout

6.1.1. Raw Data

First, drift time spectra extracted from the unprocessed data are compared. This means that the data do not have jitter correction applied. This was done using custom scripts that make histograms of the timestamps of all rising edges per channel. The comparison for single channels is shown in Fig. 6.1a. For more statistical significance the same is plotted for the sum of all drift time spectra per chamber in Fig. 6.1b. Both sets of drift time spectra are in excellent agreement.

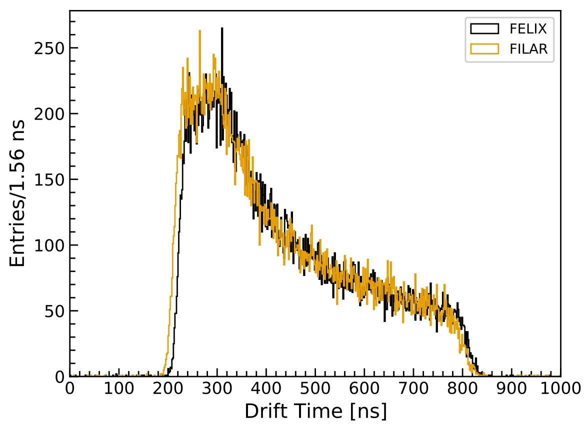

(a) Drift time spectrum of a specific single tube.

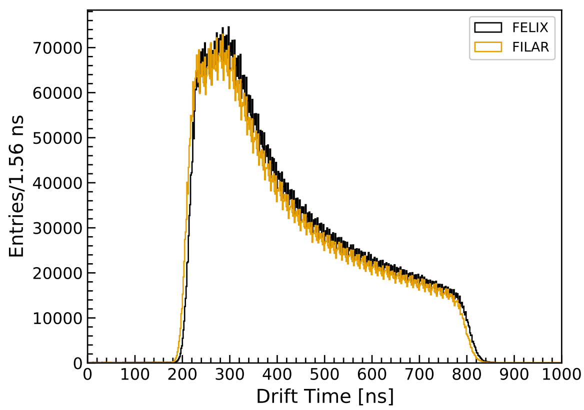

(b) Drift time spectrum, summed up per chamber.

Figure 6.1.: Comparison of the Drift Time Spectra of the two chambers, one taken with the legacy FILAR readout and one with FELIX-MROD. In (a), drift time spectra of a specific single tube from each chamber are compared. In (b), the summed drift time spectra of the two chambers are compared. In both cases, the spectra are in excellent agreement.

To compare the spectra in more detail, the drift time spectra are fitted as described in chapter 3, and for each channel the value for t_0 and $t_{\max}$ is extracted. The distributions for t_0 and $t_{\max}$ are shown in Fig. 6.2. While there are some deviations between the t_0 distributions, the $t_{\max}$ distributions are in excellent agreement. This shows that there is a systematic shift in the time stamps of approximately 7 ns between the two setups. As $t_{\max}$ is a time difference, this shift cancels.
The t_0 distribution for the FELIX-MROD readout is broader than the distribution of the FILAR values: the standard deviations are $\sigma = 3.9$ ns and 2.5 ns, respectively. This might indicate that the systematic shift is not the same for the individual drift tubes read out with the upgraded system. This discrepancy has to be investigated in the future, as it might negatively affect the track reconstruction.

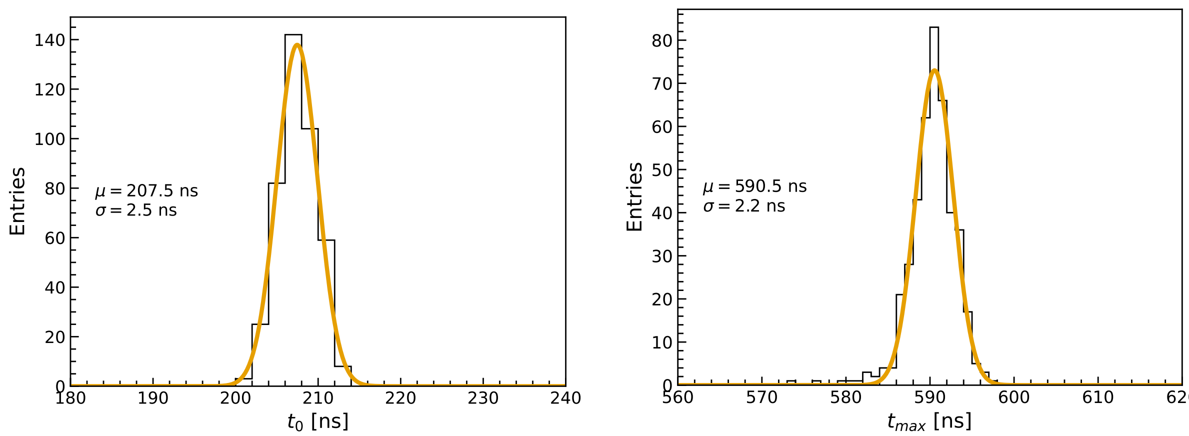

(a) t_0 and $t_{\max}$ distribution from FILAR data.

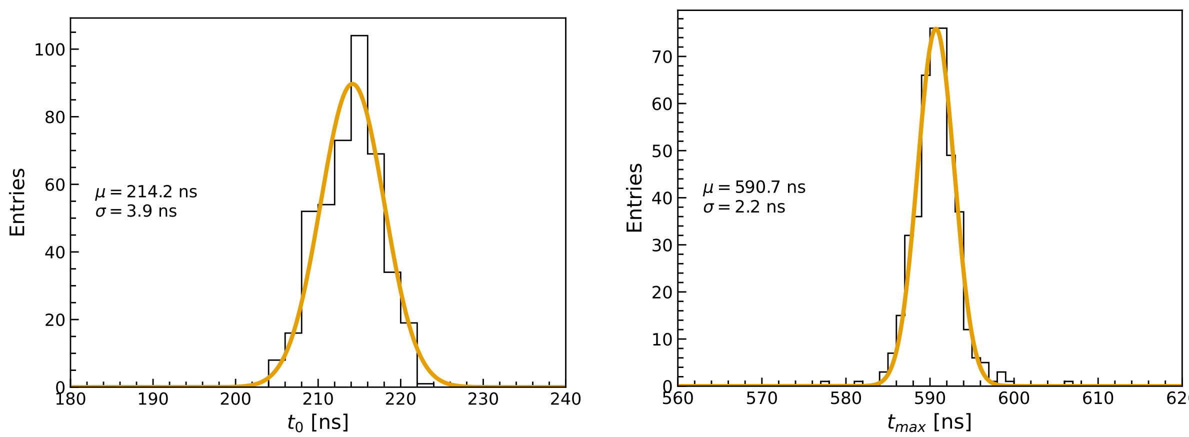

(b) t_0 and $t_{\max}$ distribution from FELIX-MROD data.

Figure 6.2.: The t_0 and $t_{\max}$ distributions for FILAR (top) and FELIX-MROD (bottom). The t_0 distribution of FELIX-MROD is shifted by approximately 7 ns with respect to the FILAR distribution. The $t_{\max}$ distributions are in excellent agreement.

In conclusion, the raw data produced by the upgraded readout agree very well with the legacy readout. The only difference that this analysis has shown is a small deviation in the absolute values of the timestamps, and can readily be corrected for by small adaptations to the `MDTEventBuilder` program.

6.1.2. Legacy Analysis Scripts

Additionally to the analysis of the raw data, the performance of the merging is investigated. As described in Chapter 5, the data produced by FELIX-MROD differ in format from the FILAR data. Therefore it is necessary to transform the data format to the FILAR standard, which also involves custom event building. This is done with the `MDTEventBuilder` program introduced in chapter 5.

To confirm its proper function one of the legacy analysis scripts is used.

For this analysis, it is treated as a black box, and its output is compared for different sets of inputs. Firstly, the script is run with only the VME file and the "real" FILAR file. Secondly, the script is called with all three files, that is with the "forged" file from the FELIX-MROD data as an additional input.

First, the influence on the FILAR drift time spectrum is investigated. In Fig. 6.3, the drift time spectrum of FILAR, as calculated by the legacy analysis script, is shown. Here, always the summed drift time spectrum of the upper multilayer is investigated. The merging with FELIX-MROD data lowers the number of entries by 8.3 %, uniformly across the spectrum. The decrease in the number of entries is to be expected, due to cases where the matching of events fails in the merging step.
For comparison, the same was done with data taken in 2021, with both chambers read out by the legacy electronics. First, the analysis script was used with only the data from the upper reference chamber, then with the data from both chambers. The decrease in events was 6.1 %. To distinguish between statistical fluctuation and a significant change in performance, more data is needed.

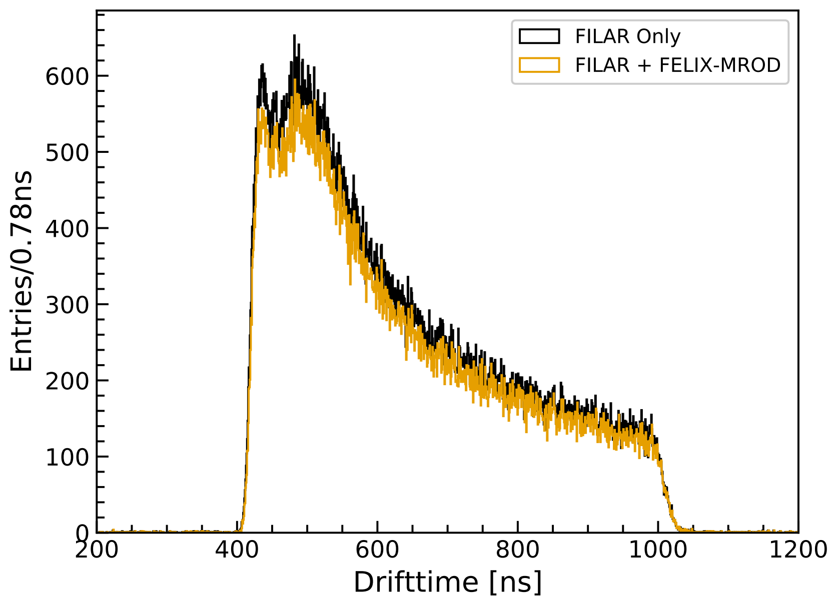

Figure 6.3.: Two FILAR drift time spectra of the upper multilayer of the upper reference chamber. The two plots were created by the legacy analysis script, before and after adding FELIX-MROD data to the input. FILAR Only refers to the analysis without FELIX-MROD data added, FILAR+FELIX-MROD to the analysis run with both chambers. With the data from the second chamber, 8.3 % of the events are lost in the merging process, uniformly across the spectrum.

Secondly, the drift time spectra produced by the analysis script are compared for the two readout systems. This is shown in Fig. 6.4. The FELIX-MROD spectrum is missing the first of the two peaks.

The first peak corresponds to muon tracks that cross the detector volume closest to the wire, within a few wire radii, and therefore have the shortest drift time. This means that they cross within the gas amplification region, and correspond to the smallest signals, which are the first to be cut by raising the ASD threshold. It is unexpected that the first peak is only missing in the FELIX-MROD setup, as in both setups data were taken with an ASD threshold set to −38 mV.

To exclude a general issue with the electronics of the lower reference chamber, additional data were taken with an ASD threshold of −32 mV for both setups. The results are depicted in Fig. 6.6. With the threshold lowered, the first peak also appears for the FELIX-MROD system. Also, the merging efficiency was determined, with 7.6 % of the events lost. This value lies between the value of 6.1 % obtained from the legacy system and 8.3 % in Fig. 6.3.

The gas supply for both chambers is the same. Other than a leak in the supply line to the lower reference chamber, this can therefore not be the cause of the difference in the setup. Another possible explanation is the different CSM cards used in the setup: it could be possible, that the configuration settings of the ASD parameters are interpreted differently in the new and the legacy CSM. A final conclusion can not be drawn here. The discrepancy has to be investigated further, with the most likely causes being a leak in the gas system or subtle differences in the JTAG protocol of the two CSM versions.

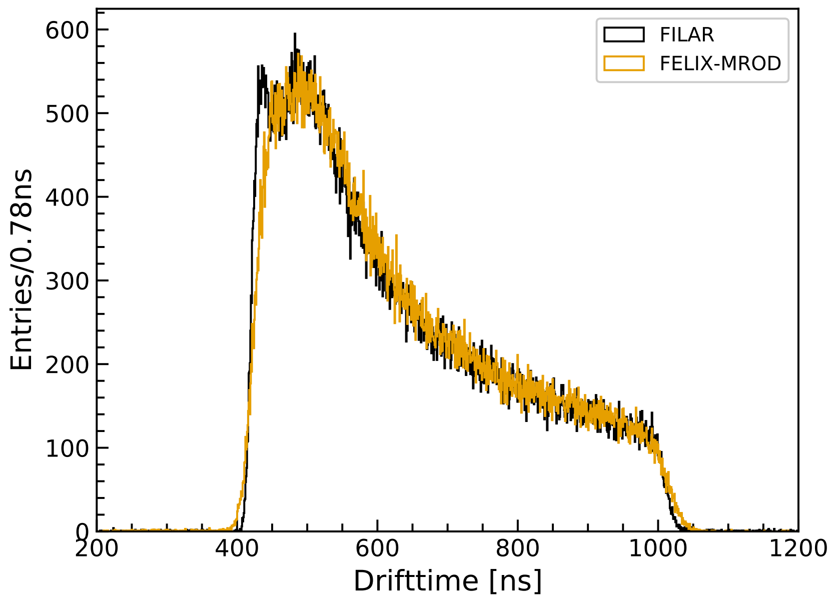

Figure 6.4.: Drift time spectra for the upper and lower reference chamber created by the legacy analysis script for both readouts. For both chambers, only the entries from the upper multilayer are shown. The FELIX-MROD data (lower chamber) are missing the first of the two peaks in the beginning. Otherwise, the spectra agree well. The data were taken with a main ASD threshold of −38 mV for both chambers.

The t_{max} fits for both readout systems, at −38 mV threshold, are shown in Fig. 6.5. They agree with the values obtained from the raw data, as expected. The jitter discussed in chapter 5 smears out the beginning and end of the spectrum equally, leading to different rise and fall times, but not to a change of the half-rise and half-fall points. The maximum drift time therefore stays the same.

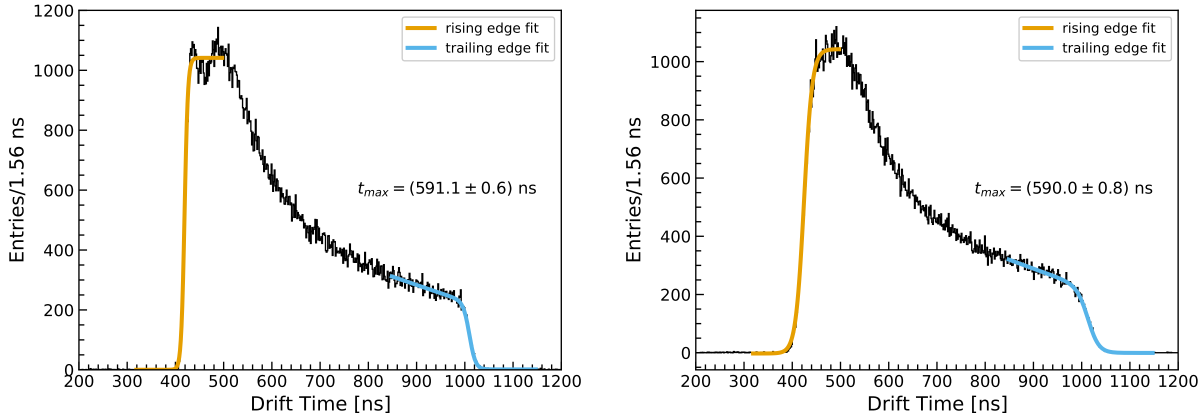

(a) Fitted drift time spectrum for the upper multi-layer of the FILAR chamber.

(b) Fitted drift time spectrum for the upper multi-layer of the FELIX-MROD chamber.

Figure 6.5.: Fitted drift time spectra for the analyzed data of the two readout systems. Even though FELIX-MROD differs slightly in shape from the FILAR data, both values for t_{max} agree with the values obtained from the raw data.

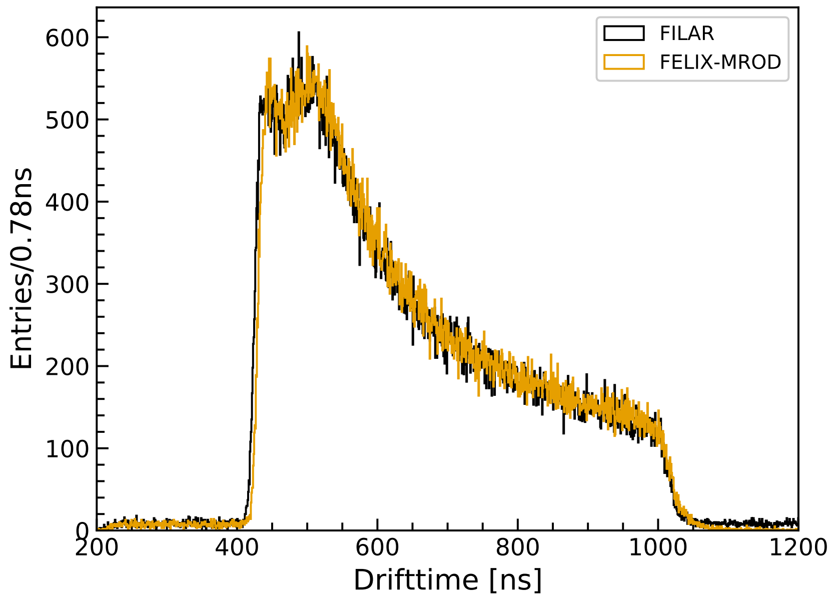

Figure 6.6.: Drift time spectra created by the legacy analysis script for both readouts, taken with a lower threshold of -32 mV. The FELIX-MROD data now show excellent agreement with FILAR.

6.2. Gas Composition

In the previous section, it has been shown that the merging of FELIX-MROD data with FILAR data works and that the drift time spectra of the two different readout systems agree very well. However, it has to be briefly mentioned that the drift time spectra collectively differ from the expectation. The maximum drift time for standard ATLAS parameters is approximately 700 ns [Levin et al. 2008]. Therefore, the drift time spectra observed here are on the order of 100 ns shorter than expected.

In [Levin et al. 2008], the dependence of t_{max} on different parameters of the gas is discussed. It is shown that the maximum drift time has a strong dependence on the mixing ratio of Ar/CO_2.

The gradient in terms of CO_2 percentage is approximately 89 ns/Vol%. By the mixing ratio being off by a little over 1 % absolute, the difference in $t_{\max}$ can be explained. The dependence on the other parameters discussed in the paper, namely temperature, pressure and water fraction is not large enough to explain the difference.

The discussion in [Levin et al. 2008] can only be taken as a first-order approximation, as the variation of the CO_2 percentage in the paper is less than 1 % absolute. An extensive study on the dependence of the drift time spectrum on the Ar/CO_2 mixing ratio was done in [Tyler 2011].

We can use the Garfield++ Simulation introduced in chapter 3 to get an estimate for the CO_2 in our system. For simplicity, we assume that the water and oxygen pollution in our system is small, close to zero. The simulation in chapter 3 was used to produce $t_{\max}$ values as a function of the CO_2 content. We now fit this with a second-order polynomial. This way, we can extract the value of the CO_2 percentage corresponding to the measured maximum drift time of $t_{\max} = 590.7$ ns. It is approximately 5.5 %, as shown in Fig. 6.7.

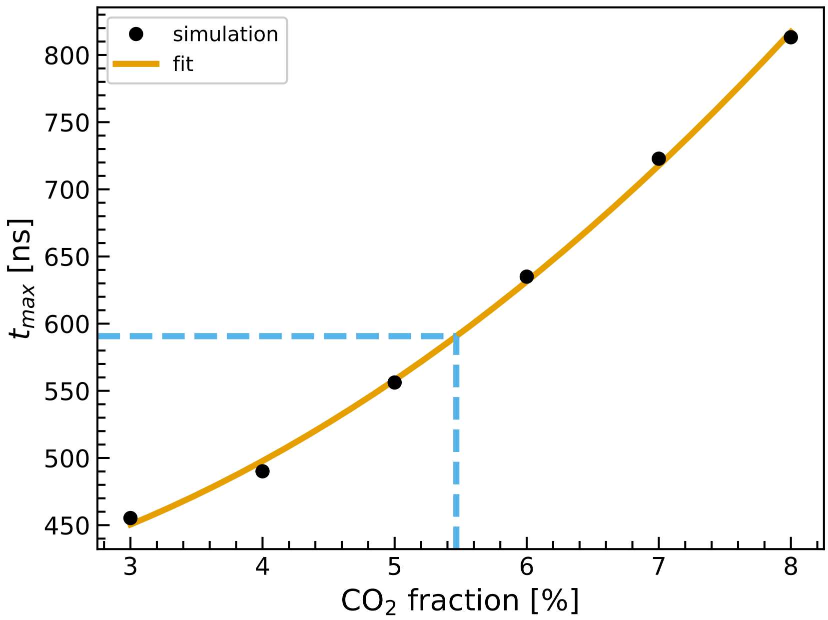

Figure 6.7.: Maximum drift time as a function of CO_2 fraction. Dashed line: The CO_2 percentage corresponding to $t_{\max} = 590.7$ ns is approximately 5.47 %.

As an additional check, we run the Garfield simulation again, with a mixing ratio of Ar/CO_2 94.5:5.5 and with $2 \cdot 10^5$ iterations. The simulated drift time spectrum is compared with the analyzed FELIX-MROD data, which was taken with -32 mV ASD threshold. This is shown in Fig. 6.8. The simulation and the measurement agree well. As was discussed in chapter 3, the shape of the drift time spectrum also depends on the CO_2 fraction. The good agreement in the shape further indicates that the CO_2 percentage is approximately 1.5 % lower than expected.

The trailing edge of the measured data in Fig. 6.8 has a longer fall time than the simulation. This is caused by a geometric effect. In the simulation the wire is perfectly in the middle of the tube, therefore the drift time of tracks close to the wall is the same for all angles. In the real detector, the wire may not be perfectly in the center. The resulting drift time spectrum is then an integral over many spectra with slightly different lengths, resulting in a gentler slope [Rauscher 2005].

In conclusion, the shorter drift time most likely is caused by a wrong Ar/CO_2 mixing ratio. This could be caused by a gas flow controller which was not properly calibrated. To confirm this, the

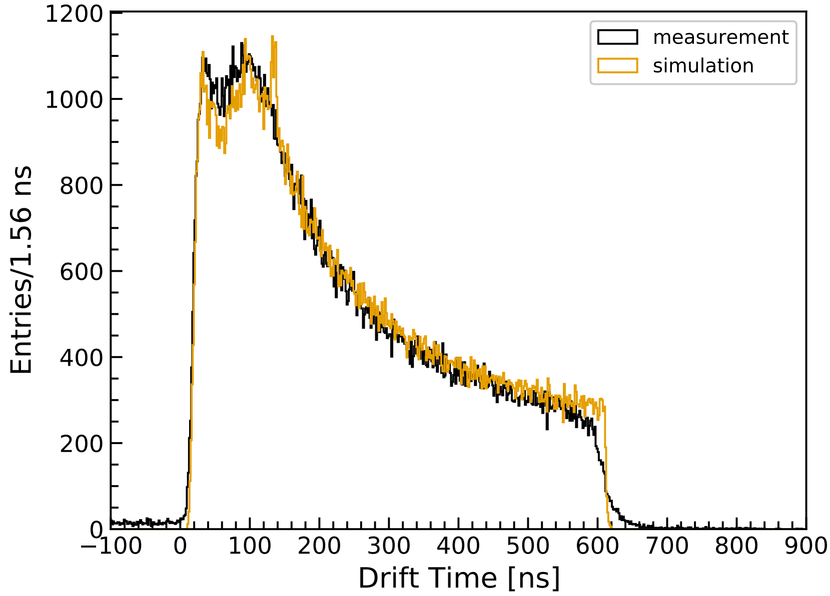

Figure 6.8.: Simulated drift time spectrum with 5.5 % CO_2 in comparison with FELIX-MROD data. The histograms are normalized to the same number of entries. Simulation and measurement agree very well.

gas mixture could be measured with a binary gas analyzer.

7. Summary and Outlook

The aim of this work was the upgrade of the Cosmic Ray Facility in Garching to the current standard of ATLAS MDT readout electronics. First, an introduction to the Phase-II Upgrade of ATLAS was given and the possible role of the Cosmic Ray Facility as a testing site was explained. Since the tests to be performed in the CRF concern the readout electronics of the MDT chambers, which are gaseous detector systems, a general discussion of the physical processes in gaseous particle detectors followed. Then, the mechanical structure of the MDT chamber was discussed, as well as the characteristics of the detector signal. The drift time spectrum was introduced as the most important quantity to gauge MDT performance. Subsequently, the readout electronics, as they are presently used in ATLAS, were presented. The upgrade of the Cosmic Ray Facility to the FELIX-MROD based readout system, which is compatible with the current ATLAS electronics, was discussed in chapter 5. In that chapter, also the measures taken for backward compatibility to the legacy readout system were included. Finally, the correct function of the upgrade and the backward compatibility were confirmed in chapter 6. The goal of the thesis is therefore achieved.

Now that the CRF is compatible with the present readout electronics, it can be used for tests of electronics compatible with the current standard of the ATLAS Muon Spectrometer. Systematic tests of the FELIX-MROD system - to conclude its research and development phase by the NIKHEF team - are planned for July 2023. Also, the mezzanine cards designed for the Phase-II upgrade have a legacy mode, which makes them compatible with the current electronics. They are also to be tested at the upgraded CRF in the near future.

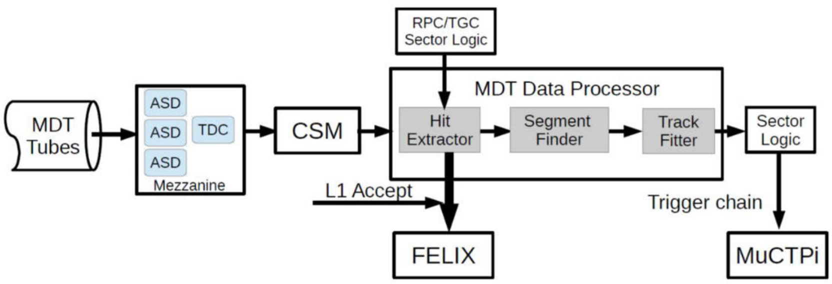

Figure 7.1.: Overview of the Phase-II MDT readout chain. Taken from [Zhu 2019].

For Phase-II tests, further upgrades are still needed. The re-designed readout chain, which is shown in Fig. 7.1, has an additional trigger step with respect to the present system. The new MDT Trigger Processor (MDTTP) board will use MDT hit information online, to reduce the output trigger rate by a factor of 3-5 at HL-LHC conditions. The algorithm uses sector logic information of the RPC/TGC trigger detectors to open a region of interest, in which the muon track segment in the chamber can then be reconstructed. The information from the three detector layers is then used to estimate the muon transverse momentum [Cieri and The ATLAS Collaboration 2022].

The first two steps of the MDTTP algorithm and the role of the sector logic are visualized in Fig. 7.2. The sector logic is needed to define a region of interest for the MDTTP board. It is possible to emulate this in the CRF by the installation of additional scintillators. The triggering

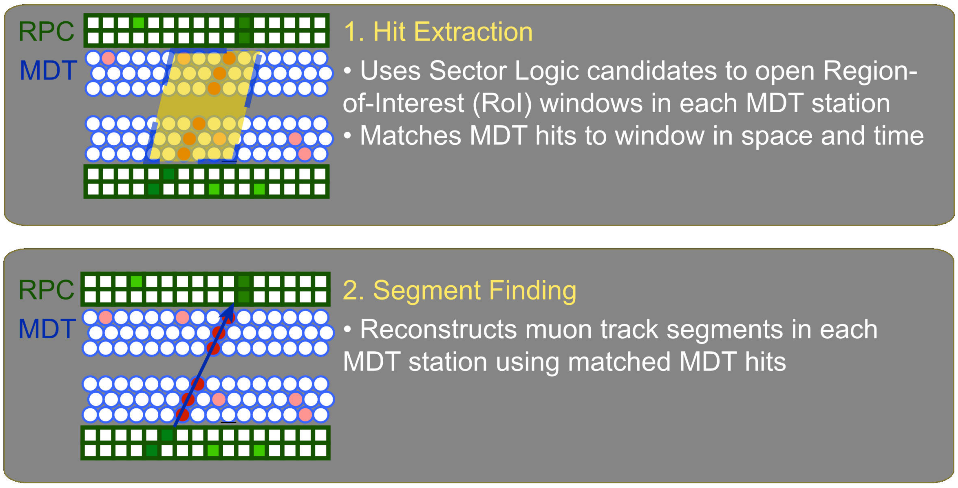

Figure 7.2.: Overview of the Phase-II MDT readout chain. Adapted from [Cieri and The ATLAS Collaboration 2022].

scintillators that are installed so far in the hodoscopes of the CRF are perpendicular to the MDT tubes. By the installation of scintillators in parallel to the tubes, the basis for a scintillator-based sector logic can be established. This is shown in Fig. 7.3. With it, the MDTTP will receive the necessary sector logic input, and the Phase-II electronics can be fully tested in the CRF.

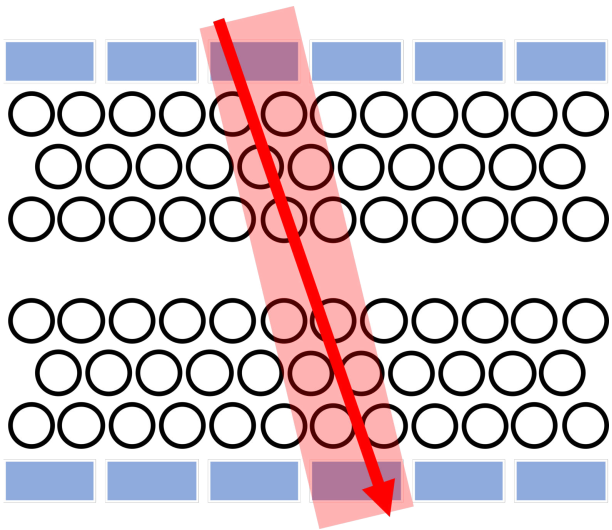

Figure 7.3.: Sketch of scintillators parallel to the MDTs. With this, it will be possible to implement a RPC/TGC sector logic emulation in the CRF. Shown is only one chamber between the scintillators. In the real setup, the scintillators will be installed on the top and bottom of the CRF.

Bibliography

Arai, Y. et al. (2008). "ATLAS Muon Drift Tube Electronics". In: *Journal of Instrumentation* 3.09, P09001. ISSN: 1748-0221. DOI: 10.1088/1748-0221/3/09/P09001.

Arai, Y. (2003). *AMT-3 User's Manual*. KEK, National High Energy Accelerator Research Organization. URL: https://twiki.cern.ch/twiki/pub/Sandbox/LiangGuanSandbox/AMT3manual.pdf (visited on Apr. 14, 2023).

ATLAS FELIX Group (2023). *FELIX User Manual*. URL: https://atlas-project-felix.web.cern.ch/atlas-project-felix/user/felix-doc/felix-user-manual/4.2.x/felix-user-manual.html (visited on Apr. 15, 2023).

ATLAS Muon Collaboration (1997). *ATLAS Muon Spectrometer: Technical Design Report*. Technical Design Report CERN/LHCC 97–22. Geneva: CERN. URL: http://atlasinfo.cern.ch/Atlas/GROUPS/MUON/TDR/pdf_final/mTDR.pdf (visited on Apr. 26, 2023).

Ball, B. et al. (2004). *CSM-0 Users Manual*. URL: https://twiki.cern.ch/twiki/pub/Sandbox/LiangGuanSandbox/CSM-0usersA4.pdf (visited on Apr. 5, 2023).

Baron, S. (2021). *The TTC Website*. Timing, Trigger and Control (TTC) Systems for the LHC. URL: http://ttc.web.cern.ch/ (visited on May 10, 2023).

Biagi, S. and Veenhof, R. (2023). *Transport of Electrons in Gas Mixtures*. URL: https://magboltz.web.cern.ch/magboltz/ (visited on May 19, 2023).

Boterenbrood, H. (2011). *MDT-DCS CANopen Module*. Amsterdam: NIKHEF. URL: https://www.nikhef.nl/pub/departments/ct/po/html/MDT/MDT-DCS-CANnode.pdf (visited on Apr. 15, 2023).

Boterenbrood, H. et al. (2006). "The Read-out Driver for the ATLAS MDT Muon Precision Chambers". In: *IEEE Transactions on Nuclear Science* 53.3, pp. 741–748. ISSN: 1558-1578. DOI: 10.1109/TNS.2006.874307.

CERN (2023). *ATLAS*. URL: https://home.cern/science/experiments/atlas (visited on May 10, 2023).

Chapman, J. et al. (2007). *CSM-4 & Final CSM Design Manual*. ATL-M-ER-0004, EDMS ID 897581. URL: https://edms.cern.ch/file/897581/1/CSM_user_Manual.pdf (visited on Apr. 5, 2023).

Cieri, D. and The ATLAS Collaboration (2022). *Upgrade of the First-Level Muon Trigger for the ATLAS Experiment at the HL-LHC*. URL: https://cds.cern.ch/record/2811302 (visited on May 13, 2023).

Engl, A. (2007). "Temperaturstudien an ATLAS-MDT-Myondetektoren". Diploma Thesis. Munich: Ludwig-Maximilians-Universität. URL: https://www.etp.physik.uni-muenchen.de/publications/theses/download/dipl_aengl.pdf (visited on May 7, 2023).

Fleischmann, P. (2020). "MDT Gas System". MDT Gas System. URL: https://indico.cern.ch/event/940281/contributions/3950904/attachments/2076286/3486452/MdtGas-20200717.pdf (visited on May 17, 2023).

Haas, S. (2005). *FILAR: Quad HOLA S-LINK to 64-Bit/66 MHz PCI Interface.* URL: https://hsi.web.cern.ch/s-link/devices/filar/welcome.html (visited on Apr. 23, 2023).

Herrmann, M. (2019). "Series Calibration of Segmented and Multi-Layered Micromegas Modules for ATLAS". PhD thesis. Munich: Ludwig-Maximilians-Universität. URL: https://www.etp.physik.uni-muenchen.de/publications/theses/download/phd_mherrmann.pdf (visited on May 8, 2023).

HL-LHC Collaboration (2023). *The HL-LHC Project.* URL: https://hilumilhc.web.cern.ch/content/hl-lhc-project (visited on Apr. 15, 2023).

König, A. (2020). "The Ageing MDT MROD System and a Possible Backup". DAQ, DCS and Operations (Muon Week Plenary Session). URL: https://indico.cern.ch/event/910596/contributions/3830735/attachments/2037661/3412149/Felix_MROD.pdf (visited on Apr. 15, 2023).

Leo, W. R. (1994). *Techniques for Nuclear and Particle Physics Experiments: A How-to Approach.* 2nd ed. Springer Berlin Heidelberg New York. ISBN: 978-3-540-57280-0.

Levin, D. S. et al. (2008). "Drift Time Spectrum and Gas Monitoring in the ATLAS Muon Spectrometer Precision Chambers". In: *Nuclear Instruments and Methods in Physics Research Section A: Accelerators, Spectrometers, Detectors and Associated Equipment* 588.3, pp. 347–358. ISSN: 0168-9002. DOI: 10.1016/j.nima.2008.01.096.

LMU Munich (2023). *Cosmic Ray Facility - Elementary Particle Physics - LMU Munich.* URL: https://www.etp.physik.uni-muenchen.de/research/detector-development/cosmic/index.html (visited on Apr. 4, 2023).

LXCAT (2023). *Morgan Database.* URL: www.lxcat.net (visited on Apr. 11, 2023).

Melissinos, A. (1966). *Experiments in Modern Physics.* Academic Press. ISBN: 978-0-12-489850-9.

Nicolás Viaux, M. (2023). "The ATLAS 'New Small Wheel' Muon Detector Stations Recently Commissioned for LHC Run3". In: *Nuclear Instruments and Methods in Physics Research Section A: Accelerators, Spectrometers, Detectors and Associated Equipment* 1045, p. 167574. ISSN: 0168-9002. DOI: 10.1016/j.nima.2022.167574.

Particle Data Group et al. (2022). "Review of Particle Physics". In: *Progress of Theoretical and Experimental Physics* 2022.8. ISSN: 2050-3911. DOI: 10.1093/ptep/ptac097. eprint: https://academic.oup.com/ptep/article-pdf/2022/8/083C01/49175539/ptac097.pdf.

Posch, C., Hazen, E., and Oliver, J. (2007). *MDT-ASD, CMOS Front-End for ATLAS MDT.* ATL-MUON-2002-003. Geneva: CERN. URL: https://cds.cern.ch/record/684217 (visited on Apr. 14, 2023).

Ramsauer, C. (1921). "Über Den Wirkungsquerschnitt Der Gasmoleküle Gegenüber Langsamen Elektronen". In: *Annalen der Physik* 369.6, pp. 513–540. ISSN: 1521-3889. DOI: 10.1002/andp.19213690603.

Rauscher, F. (2005). "Untersuchung Des Verhaltens von Driftrohren Bei Starken Gamma-Bestrahlung Sowie Vermessung von Driftrohrkammern Mit Hilfe von Myonen Der Kosmischen Höhenstrahlung". PhD thesis. Munich: Ludwig-Maximilians-Universität. URL: https://www.etp.physik.uni-muenchen.de/publications/theses/download/phd_frausch.pdf (visited on May 6, 2023).

Sauli, F. (2023). *Gaseous Radiation Detectors: Fundamentals and Applications.* Cambridge Monographs on Particle Physics, Nuclear Physics and Cosmology. Cambridge: Cambridge University Press. ISBN: 978-1-00-929118-7. DOI: 10.1017/9781009291200.

Schindler, H. (2023a). *Garfield++ User Guide*. User Guide. URL: https://garfieldpp.web.cern.ch/documentation/UserGuide.pdf (visited on Apr. 26, 2023).

– (2023b). *Garfield++*. URL: https://garfieldpp.web.cern.ch/garfieldpp/ (visited on Apr. 26, 2023).

Smirnov, I. B. (2005). "Modeling of Ionization Produced by Fast Charged Particles in Gases". In: *Nuclear Instruments and Methods in Physics Research Section A: Accelerators, Spectrometers, Detectors and Associated Equipment* 554.1, pp. 474–493. ISSN: 0168-9002. DOI: 10.1016/j.nima.2005.08.064.

– (2018). *Modeling of Ionization Produced by Fast Charged Particles in Gases*. URL: http://ismirnov.web.cern.ch/ismirnov/heed (visited on May 19, 2023).

Steerenberg, R. (2018). *LHC Report: Protons: Mission Accomplished*. URL: https://home.cern/news/news/physics/lhc-report-protons-mission-accomplished (visited on May 10, 2023).

The ATLAS Collaboration (2008). "The ATLAS Experiment at the CERN Large Hadron Collider". In: *Journal of Instrumentation* 3.08, S08003. DOI: 10.1088/1748-0221/3/08/S08003.

– (2017). *Technical Design Report for the Phase-II Upgrade of the ATLAS Muon Spectrometer*. CERN-LHCC-2017-017, ATLAS-TDR-026. Geneva: CERN. URL: https://cds.cern.ch/record/2285580.

– (2019). "Resolution of the ATLAS Muon Spectrometer Monitored Drift Tubes in LHC Run 2". In: *Journal of Instrumentation* 14.09, P09011. ISSN: 1748-0221. DOI: 10.1088/1748-0221/14/09/P09011.

Tyler, N. (2011). "Studies on Linear and Fast Drift Gases for ATLAS MDT Chambers". Master Thesis. Munich: Ludwig-Maximilians-Universität. URL: https://www.etp.physik.uni-muenchen.de/publications/theses/download/master_ntyler.pdf (visited on Apr. 24, 2023).

Veenhof, R. (1998). "Garfield, Recent Developments". In: *Nuclear Instruments and Methods in Physics Research Section A: Accelerators, Spectrometers, Detectors and Associated Equipment* 419.2, pp. 726–730. ISSN: 0168-9002. DOI: 10.1016/S0168-9002(98)00851-1.

Zhu, J. (2019). *The Phase-II Upgrade of the ATLAS Muon Spectrometer*. Geneva. DOI: 10.22323/1.367.0070.

A. Abbreviations

ASD	Amplifier/Shaper/Discriminator
ATLAS	A Toroidal LHC ApppraratuS
CERN	European Organization for Nuclear Research
CRF	Cosmic Ray Facility
CSM	Chamber Service Module
DCS	Detector Control System
ELMB	Embedded Local Monitor Board
FELIX	FrontEnd Link eXchange
FIFO	First In First Out
HL-LHC	High Luminosity LHC
LHC	Large Hadron Collider
MDT	Monitored Drift Tube
MDTTP	MDT Trigger Processor
Micromegas	Micromesh Gaseous Structure
MROD	MDT Read Out Driver
NSW	New Small Wheel
SM2	Small Module 2
TDC	Time to Digital Converter

B. How to Use the Updated CRF

This is a short how to take data with the Cosmic Ray Facility in the status presented in this thesis.[1] This means that the upper MDT chamber is still read out by the legacy setup, and the lower chamber by the upgraded FELIX-MROD based setup. First, the necessary steps fo the data acquisition are presented. Afterward, a short introduction to the analysis with `MDTEventBuilder` is given.

B.1. Data Taking

Step 1: Configure Legacy CSM

On `etpsc05`, open terminal in `/export/data/etpsc05` as user `etpdaq`.

1. If connected via ssh: run `export TERM=xterm`
2. Run `mtsa` to load the correct architecture environment.
3. Run `JtagProxy -n <CAN Node>`. Here, `<CAN Node>` has to be replaced with the CAN Node Address of the MDT-DCS box, see Fig. 4.3. For the upper chamber with legacy readout, the CAN Node Address is 34.

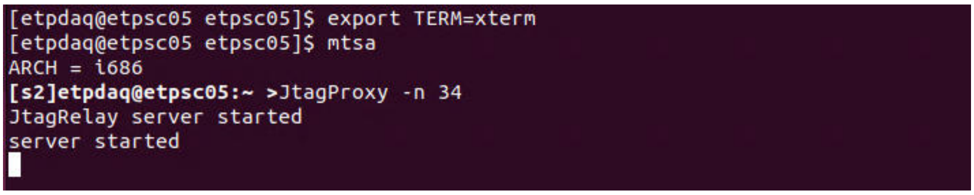

Figure B.1.: The terminal window on `etpsc05` after Step 1. The command `export TERM=xterm` only has to be run if the connection to the PC is made via ssh.

On `etpxp04` as user `etpdaq`, on the desktop.

1. Open `JtagRelay22 (2)` via the icon on the desktop.
   (Path: `C:\DAQ\Run\Jtag\Jtag\v22\JtagRelay22.exe`)

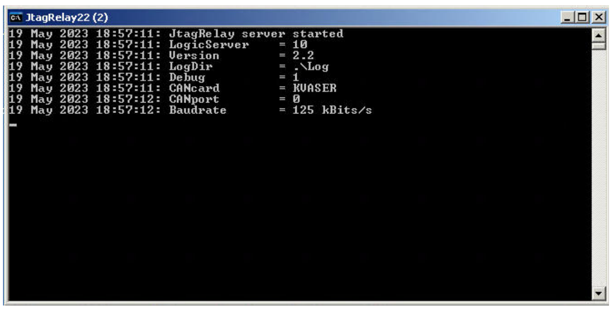

Figure B.2.: `JtagRelay22 (2)` after program start.

[1]A maintainable version is available on `https://gitlab.physik.uni-muenchen.de/crf-upgrade/how-tos`.

2. Open `DAQControl` via the icon on the desktop. This starts MiniDAQ and an output window.
   (Path: `C:\DAQ\MiniDAQ005.5\DAQControl.exe`)

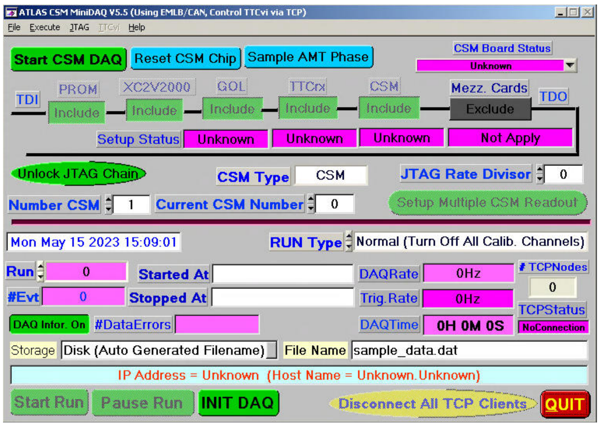

(a) MiniDAQ after the program start. The application can be closed with the `QUIT` button in the lower right.

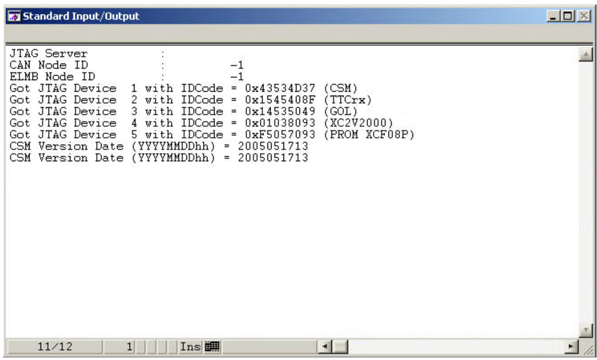

(b) The output window of MiniDAQ after starting the program.

Figure B.3.: MiniDAQ after the program start.

3. Click `INIT DAQ`. Wait until `DAQ initialization done` is written to the output window.

4. Optional: The `JTAG` option of the menu bar can now be used for parameter changes of the CSM and mezzanine cards.

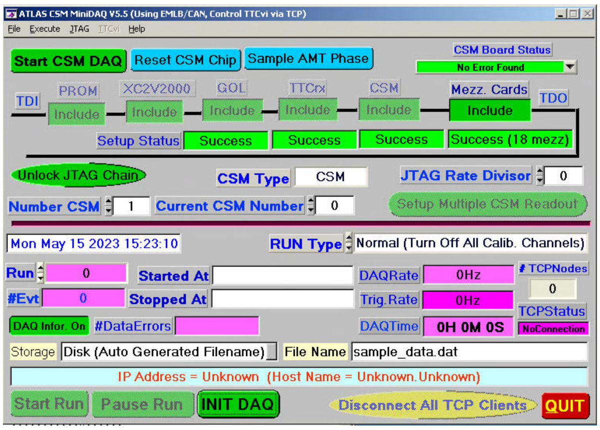

(a) MiniDAQ after executing `INIT DAQ`. The CSM and mezzanine card parameters can now be changed in the JTAG option of the menu bar.

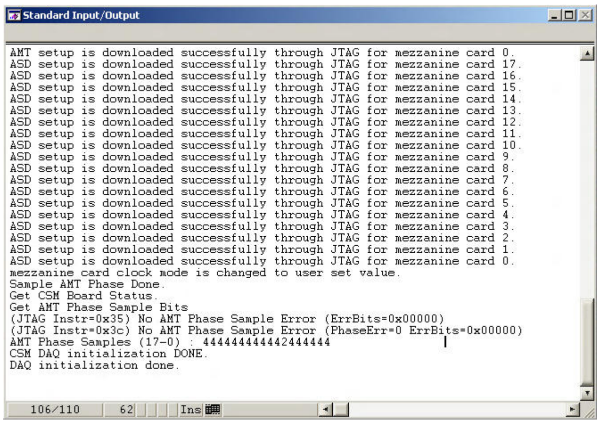

(b) The output window of MiniDAQ after executing `INIT DAQ`.

Figure B.4.: MiniDAQ after executing `INIT DAQ`.

5. Click `START CSM DAQ`, wait until `CSM DAQ Started!` is written to the output window.

6. Now that the DAQ is started, close `MiniDAQ` and `JtagRelay22`. The error message shown in Fig. B.5 will appear on quitting `MiniDAQ`. Confirm with `OK`.

7. On `etpsc05`, quit `JtagProxy` with `Ctrl+C`.

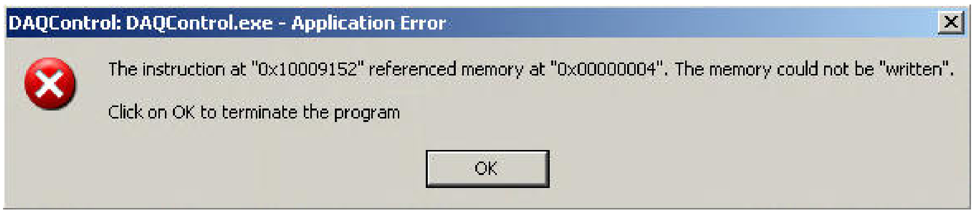

Figure B.5.: MiniDAQ error message. No need to worry, this always happens.

Step 2: Configure Updated CSM

On `gar-ex-etp09atl`, open terminal in `/home/etpdaq/csm-configurator` as user `etpdaq`.

1. `source setup.sh`
2. `cd Configurator`
3. `./csm_configurator -m 3FFFF -e -r`

Parameters for the CSM and mezzanine boards are defined in `jtag_definitions` and can be set in `test_setup`. Look at the source code of `csm_configurator` for more information. The parameter sets the mask for the mezzanine cards to address. If all 18 mezzanine cards are connected, the mask is `3FFFF`, since that corresponds to 18 1's in binary. If mezzanine cards 0 and 1 are disconnected, the mask would be `3FFFC`.

Step 3: Start FELIX-MROD

On `gar-ex-etp09atl`, open a new terminal in `/home/etpdaq/FELIX` as user `etpdaq`.

1. `source setup.sh`
2. `flx-init`
3. `source felix-scripts/reset_felixmrod.sh -r`
4. `source felix-scripts/start_felixmrod.sh`
5. Start DAQ with `fdaq -d 1 -t <time> <path/filename>`, where `<time>` is the DAQ time in seconds and `<path/filename>` is the output path. For more information run `fdaq --help`.

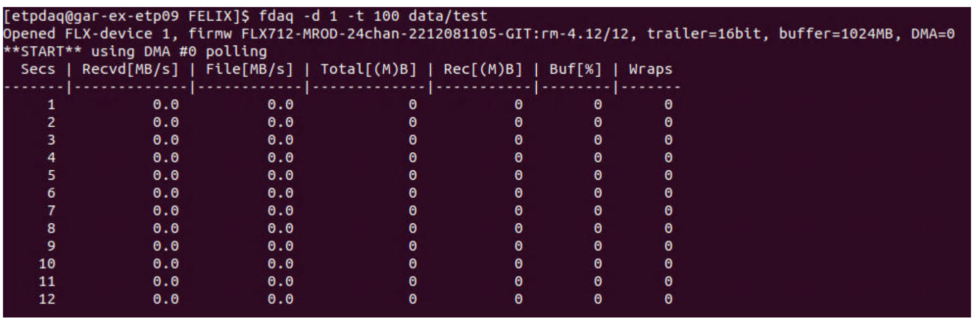

Figure B.6.: The `fdaq` program after startup, when no data are arriving. When the DAQ of the old setup is started, data will start arriving in fdaq.

Step 4: Start MT-Online

On etpsc05, same terminal as before.

1. cd /export/data/etpsc05/daq_work
2. MT-Online onechamber_n34.MT-Online <path/filename>. Sometimes, MT-Online stops after 2000 events, complaining about a FILAR issue. If this happens, etpsc05 has to be shut down and booted again after a few minutes.

If everything was done correctly, data should now be arriving at fdaq.

Secs	Recvd[MB/s]	File[MB/s]	Total[(M)B]	Rec[(M)B]	Buf[%]	Wraps
41	0.3	0.2	10.2	10.2	0	0
42	0.2	0.2	10.4	10.4	0	0
43	0.3	0.3	10.7	10.7	0	0
44	0.2	0.2	10.9	10.9	0	0
45	0.2	0.2	11.2	11.1	0	0
46	0.2	0.3	11.4	11.4	0	0
47	0.2	0.2	11.6	11.6	0	0
48	0.3	0.3	11.9	11.9	0	0
49	0.3	0.3	12.2	12.1	0	0

Figure B.7.: The fdaq program output when data is arriving.

Step 5: Stop DAQ

The program fdaq on gar-ex-etp09atl will stop after the specified time. Afterward, the data taking on etpsc05 with MT-Online has to be stopped manually with Ctrl+C.

Two files are produced on etpsc05 in /export/data/etpsc05/daq_work/<path>: <filename> and <filename>.ttcvi.0.filar. On gar-ex-etp09atl, the file <filename>.dat is produced by the FELIX-MROD setup in <path>.

B.2. Analysis

Convert FELIX-MROD file to FILAR format

To convert the FELIX-MROD file to the FILAR format, copy the <filename>.dat file to a PC where the MDTEventBuilder repository is installed. Let's assume the file is in the same directory as MDTEventBuilder.py. If they are not, use the relative paths to MDTEventBuilder.py and <filename>.dat.

1. module load marabou
2. module load python
3. python MDTEventBuilder.py <filename>.dat.

A file in the FILAR format <filename>.ttcvi.1.filar is produced. Also a root file containing the drift time spectra of the 432 tubes of the BOS chamber is produced.

To merge <filename>.ttcvi.1.filar with the analysis scripts, the VME file produced by MT-Online has to be altered: it has a colon-separated list of the .filar files produced by

`MT-Online` in its header. The `<filename>.ttcvi.1.filar` file needs to be added. For an example with the `<filename>` `test_legacyASDParams_03052023`, the header of the VME file before and after adding `<filename>.ttcvi.1.filar` is shown in Fig. B.8.

```
#BEGIN_HEADER
#VERSION_CODE 1
#TIME 1683142606
#BEGIN_MODULES
MT_VN1488S_Simple tdc1 1f_faf5_837_1037_1
MT_VN1488S_Simple tdc2 1f_faf5_837_102e_1
MT_VN1488S_Simple ttcorr 1f_faf5_837_103b_0
MT_CAEN_V775N tdc_trigtag 1f_370_4_0
MT_TTCvi ttcvi test_legacyASDParams_03052023.ttcvi.0.filar:::
#END_MODULES
```

(a) VME header as produced by `MT-Online` with one chamber read out by the legacy system.

```
#BEGIN_HEADER
#VERSION_CODE 1
#TIME 1683142606
#BEGIN_MODULES
MT_VN1488S_Simple tdc1 1f_faf5_837_1037_1
MT_VN1488S_Simple tdc2 1f_faf5_837_102e_1
MT_VN1488S_Simple ttcorr 1f_faf5_837_103b_0
MT_CAEN_V775N tdc_trigtag 1f_370_4_0
MT_TTCvi ttcvi test_legacyASDParams_03052023.ttcvi.0.filar:test_legacyASDParams_03052023.ttcvi.1.filar::
#END_MODULES
```

(b) VME header after adding the file produced by`MDTEventBuilder`.

Figure B.8.: VME header file `test_legacyASDParams_03052023` before and after adding the file produced from the FELIX-MROD data.

The legacy analysis scripts are available for the user `etpdaq` on the workstation machines `gar-ws-etp*` in `/home/e/etpdaq/etpdaqsvn/CRFscripts`. The script used in this work is `startMDTanalysis_work.sh`.

Selbstständigkeitserklärung

Hiermit erkläre ich, die vorliegende Arbeit selbständig verfasst zu haben und keine anderen als die in der Arbeit angegebenen Quellen und Hilfsmittel benutzt zu haben.

München, 22. Mai 2023 ....